

1

[ATLAS Semivisible Jets]

2

[Elena Laura Busch]

3

Submitted in partial fulfillment of the
requirements for the degree of
Doctor of Philosophy
under the Executive Committee
of the Graduate School of Arts and Sciences

4

5

6

7

8

COLUMBIA UNIVERSITY

9

2024

10

© 2024

11

[Elena Laura Busch]

12

All Rights Reserved

13

Abstract

14

[ATLAS Semivisible Jets]

15

[Elena Laura Busch]

16

Abstract of dissertation (place-holder).

Table of Contents

18	Acknowledgments	vii
19	Dedication	viii
20	Introduction or Preface	1
21	Chapter 1: The Standard Model	2
22	1.1 Phenomenology: Particles and Forces	2
23	1.1.1 Particles	2
24	1.1.2 Forces	3
25	1.2 QCD and Jets	6
26	1.3 Symmetries	7
27	1.3.1 Spontaneous Symmetry Breaking and The Higgs Mechanism	8
28	1.4 Experimental Validation of the Standard Model	9
29	1.5 Limitations of the Standard Model	10
30	Chapter 2: Physics Beyond the Standard Model	12
31	2.1 Hidden Valley Models	12
32	2.2 Dark QCD	13
33	2.3 Semi-visible Jets	14

34	Chapter 3: The Large Hadron Collider	16
35	3.1 Accelerator Physics	17
36	3.1.1 The Journey of a Proton	17
37	3.1.2 Magnets	18
38	3.2 Luminosity	19
39	3.3 LHC Timeline	22
40	Chapter 4: The ATLAS Detector	24
41	4.1 Coordinate System and Geometry	24
42	4.2 Inner Detector	26
43	4.2.1 Pixel Detector	26
44	4.2.2 Semiconductor Tracker	27
45	4.2.3 Transition Radiation Tracker	27
46	4.3 Calorimeters	28
47	4.3.1 Liquid Argon Calorimeter	29
48	4.3.2 Tile Calorimeter	32
49	4.4 Muon Spectrometer	33
50	4.5 Magnet System	35
51	4.6 Forward Detectors	36
52	4.7 Trigger and Data Acquisition	37
53	Chapter 5: Particle Reconstruction and Identification	39
54	5.1 Inner Detector Tracks	39
55	5.2 Photons and Electrons	41

56	5.3 Muons	43
57	5.4 Jets	44
58	5.4.1 Calorimeter Clusters	44
59	5.4.2 Particle Flow Reconstruction	44
60	5.4.3 Jet Clustering	44
61	5.4.4 Jet Substructure	44
62	5.5 Missing Transverse Energy	44
63	Conclusion or Epilogue	46
64	References	50
65	Appendix A: Experimental Equipment	54
66	Appendix B: Data Processing	55

List of Figures

68	1.1	Diagram of the 17 particles comprising the Standard Model	3
69	1.2	Fundamental particle interactions of the three fundamental forces described by the	
70		Standard Model [2].	5
71	1.3	An example Feynmann diagram of jet production	6
72	1.4	An illustration of the “hat shaped” potential of the Higgs field, resulting in a non-	
73		zero vacuum expectation value.	8
74	2.1	Illustration of the hidden valley potential	13
75	2.2	The massive mediator particle Z' of the s-channel realization of a HV model . . .	13
76	3.1	The LHC accelerator complex at CERN [27]	18
77	3.2	The octants of the LHC and location of various beam activities [26]. Stars indicate	
78		the locations of beam collisions, and the associated detectors recording the	
79		outcome of those collisions.	19
80	3.3	(Left) Total integrated luminosity over the course of Run 2. (Right) Average num-	
81		ber of $p\bar{p}$ interactions per bunch crossing in Run 2. Each curve is weighted by the	
82		integrated luminosity for the year.	21
83	3.4	Timeline of LHC and HL-LHC activities [29]. Integrated luminosity estimates are	
84		approximate, and not reflective of the exact amount delivered to each experiment. .	23
85	4.1	ATLAS coordinate system and geometry	26
86	4.2	A 3D visualization of the structure of the ID in the barrel region [33]	27
87	4.3	ATLAS calorimetery system [34]	28

88	4.4	Diagram of a segment of the EMB, demonstrating the accordion plate arrangement [35]	30
89			
90	4.5	A LAr pulse as produced in the detector (triangle) and after shaping (curve) [35] . .	31
91			
92	4.6	Readout gap structure in HEC [35]	31
93			
94	4.7	TileCal wedge module [38]	33
95			
96	4.8	Cross section view of the muon spectrometer system [39]	34
97			
98	4.9	Layout of the barrel and endcap toroid magnets [32]	36
99			
100	5.1	Graphic illustrating the various objects and high level features identified by ATLAS object reconstruction, and their interaction with different systems of the ATLAS detector [42]	40
101			
102	5.2	Track reconstruction seeding, finding and fitting illustration [43]	41
103			
104	5.3	Four types of muon track candidates [45].	42
105			
106	5.4	Four types of muon track candidates [47].	45
107			

List of Tables

102

Acknowledgements

103 Insert your acknowledgements text here. This page is optional, you may delete it if not
104 needed.

105

Dedication

106

Dedicated to my friends and family

107

Introduction or Preface

108 Insert your preface text here if applicable. This page is optional, you may delete it if not
109 needed. If you delete this page make sure to move page counter comment in thesis.tex to correct
110 location.

111

112

Chapter 1: The Standard Model

113 The Standard Model of particle physics is a universally accepted framework which explains
114 the interactions of fundamental particles. All known fundamental particles, outlined in Figure
115 1.1, are represented in the Standard Model. The model describes three of the four known forces:
116 the electromagnetic force, the weak force, and the strong force. Gravity, the fourth fundamental
117 force, is not addressed by the Standard Model. The Standard Model was primarily developed over
118 the course of the 1960s and 1970s, by combining the work of many physicists into one coherent
119 model. The Standard Model has been established as a well-tested theory by decades of experimen-
120 tal physics research.

121 This chapter will seek to introduce the phenomenology and mathematical foundations of the
122 Standard Model, and present the supporting experimental evidence. Phenomenon which are unex-
123 plained by the Standard Model such as gravity will be considered at the end of the chapter, leading
124 to an exploration of theories beyond the Standard Model in the subsequent chapter.

125 1.1 Phenomenology: Particles and Forces

126 1.1.1 Particles

127 A classic representation of the particles comprising the Standard Model is shown in Figure
128 1.1. The two primary particles classes are bosons (gauge bosons and the scalar Higgs boson) and
129 fermions (leptons and quarks). The bosons are carriers of fundamental forces, while the fermions
130 are the building blocks of matter. Fermions are sorted into three *generations*, and each fermion is
131 identified by a unique *flavor*.

132 Each entry in the table in Figure 1.1 is accompanied by 3 characteristic numbers: mass, charge,
133 and spin. The mass of each particle is determined to limited precision by experimental observa-

Standard Model of Elementary Particles

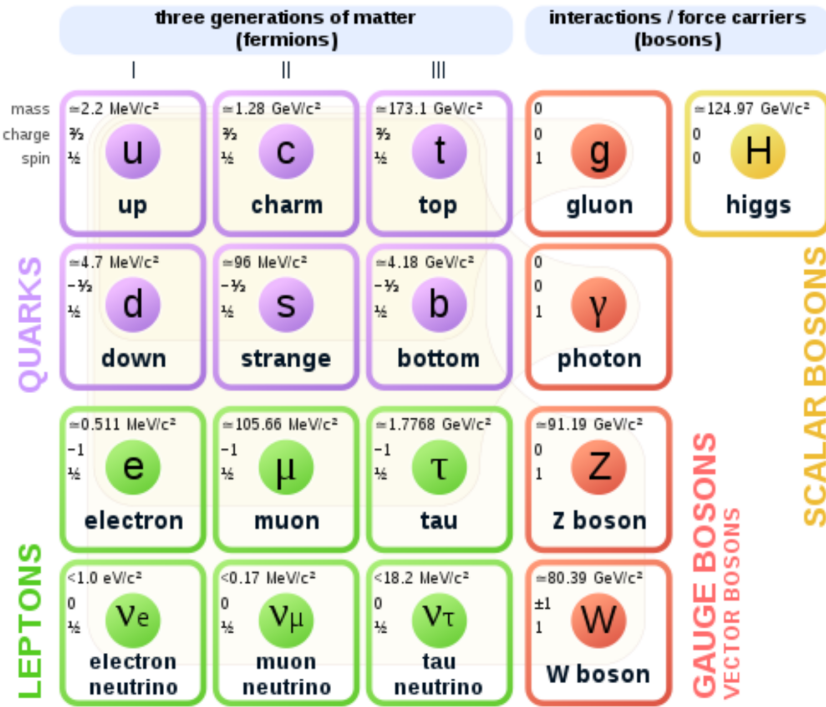


Figure 1.1: Diagram of the 17 particles comprising the Standard Model

134 tion, with the exception of photons and gluons which are known to be massless. Charge refers to
 135 the electromagnetic charge in the case of leptons and W bosons, and to color charge in the case
 136 of quarks and gluons. Spin is an intrinsic form of angular momentum carried by fundamental
 137 particles; all fermions have half integer spin, while bosons have integer spin.

138 Each particle is also known to have an *antiparticle*. Each antiparticle has the same mass but the
 139 opposite charge of their Standard Model counter part; for example, the antiparticle of the electron
 140 is the positron, which has all the same properties but a positive charge. The photon, Z boson,
 141 and Higgs are each their own antiparticle. The nature of antineutrinos is an open question driving
 142 neutrino physics research, as it is not currently known whether neutrinos are their own antiparticle.

143 1.1.2 Forces

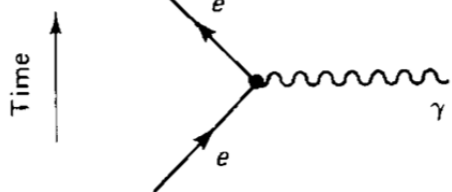
144 The three fundamental forces explained by the Standard Model are the electromagnetic force,
 145 the strong force, and the weak force. The photon is the carrier of the electromagnetic force, which

¹⁴⁶ dictates the nature of interactions between electrically charged particles, and is widely covered by
¹⁴⁷ introductory physics courses. The electromagnetic force has an infinite interaction range, a result
¹⁴⁸ of the massless and non-self interaction nature of the photon. The electromagnetic interaction is
¹⁴⁹ described by the theory of quantum electrodynamics (QED).

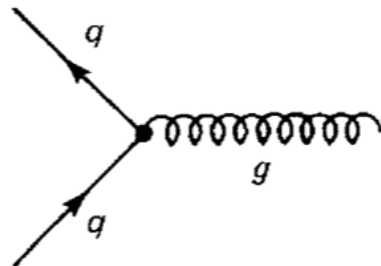
¹⁵⁰ The weak force gives rise to atomic radiation and decay. It allows for the processes of beta
¹⁵¹ decay, which enables conversion between neutrons and protons within the nucleus of an atom. In
¹⁵² the process of beta decay, a proton decays into a neutron, a positron, and a neutrino; or, a neutron
¹⁵³ decays into a proton, an electron and an antineutrino. The weak interaction allows for quark flavor
¹⁵⁴ mixing, the which enables beta decay. The W^+ , W^- , and Z^0 are the force carriers of the weak force.
¹⁵⁵ The effective range of the weak force is limited to subatomic distances, as a result of the massive
¹⁵⁶ nature of the mediator bosons. The unified theory of the electroweak interaction posits that at high
¹⁵⁷ enough energies the electromagnetic interaction and the weak force merge into the same force.
¹⁵⁸ This threshold is termed the unification energy and calculated to be about 246 GeV [1].

¹⁵⁹ The strong force confines quarks into hadron particles, such as protons and neutrons. The
¹⁶⁰ strong force also allows for the creation of atomic nuclei by binding protons and neutrons together,
¹⁶¹ and is generally referred to as the “nuclear force” in this context. The gluon is the mediator of
¹⁶² the strong force, which is a short-range force which acts at subatomic distances on the order of
¹⁶³ 10^{-15} m. At this range, the strong force is about 100x as strong as the electromagnetic force,
¹⁶⁴ which allows for the creation of positively charged nuclei [2]. The strong force is described by the
¹⁶⁵ theory of quantum chromodynamics (QCD). In the same way that QED dictates the interaction of
¹⁶⁶ electrically charges particles, QCD dictates the interactions of *color-charged* particles. Due to the
¹⁶⁷ particular importance of QCD in this thesis, this topic will be explored in detail in section 1.2.

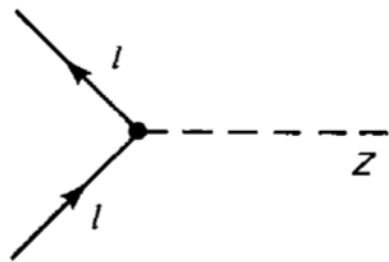
¹⁶⁸ The fundamental Feynmann diagram for each of the three forces discussed here is depicted
¹⁶⁹ in Figure 1.2. The fourth fundamental force, gravity, is not currently explained by any known
¹⁷⁰ mechanism within the Standard Model.



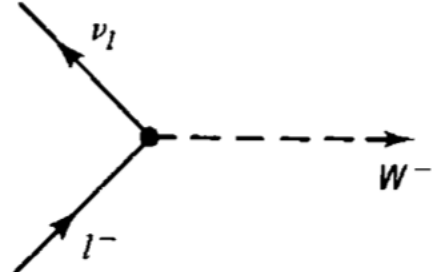
(a) The electromagnetic force



(b) The strong force



(c) The neutral weak force



(d) The charged weak force

Figure 1.2: Fundamental particle interactions of the three fundamental forces described by the Standard Model [2].

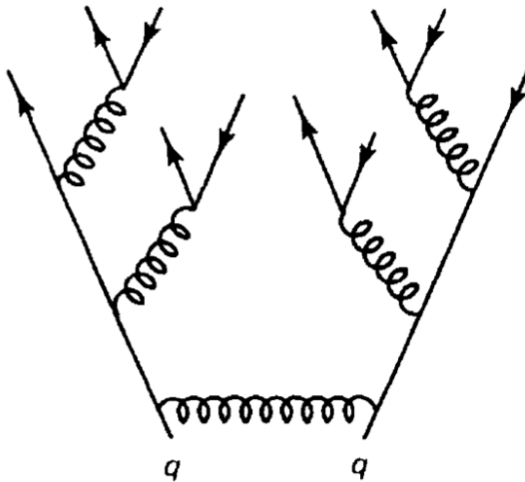


Figure 1.3: An example Feynmann diagram of jet production

¹⁷¹ 1.2 QCD and Jets

¹⁷² While there is only one type of electric charge, there are three types of color charge; red, green,
¹⁷³ and blue. In the process $q \rightarrow q + g$, the color of the quark can change. In order to conserve color
¹⁷⁴ charge, gluons are bicolored, and always carry some positive color charge and some negative color
¹⁷⁵ charge.

¹⁷⁶ Color charged particles can only exist in bound states which result in a neutral total color
¹⁷⁷ charge, a principle known as confinement. This requires that quarks and gluons exist in group
¹⁷⁸ states known as hadrons; either mesons in the case of two quarks or baryons in the case of three
¹⁷⁹ quarks. When a quark is separated from a hadron, confinement dictates that other colored objects
¹⁸⁰ are produced around the quark to obey confinement. An example of this process is shown in
¹⁸¹ Figure 1.3. This ensemble of objects, generally a mixture of quarks and gluons, is termed a *jet*.
¹⁸² Jets are among the most common phenomenon observed by detectors at hadron colliders, and their
¹⁸³ complex structure makes them a key focus of many physics analyses.

¹⁸⁴ **1.3 Symmetries**

¹⁸⁵ The Standard Model is a renormalizable quantum field theory that obeys the local symmetry

¹⁸⁶ G_{SM} :

$$G_{SM} = SU(3)_C \times SU(2)_L \times U(1)_Y. \quad (1.1)$$

¹⁸⁷ The $SU(3)_C$ symmetry component represents the non-Abelian gauge group of QCD. There
¹⁸⁸ are 8 generators for the $SU_C(3)$ group which correspond to 8 types of gluon, each representing a
¹⁸⁹ different superposition of color charge [3]. The $SU(2)_L \times U(1)_Y$ symmetry group represents the
¹⁹⁰ electroweak sector of the Standard Model, which can be spontaneously broken into the electromag-
¹⁹¹ netic and weak sectors. There are 4 generators for this group, which correspond to four massless
¹⁹² gauge bosons W^1 , W^2 , W^3 , and B . From these massless gauge bosons are formed the massive
¹⁹³ mediators of the weak force, the W^- , W^+ and Z^0 bosons, and the massless electromagnetic force
¹⁹⁴ carrier, the photon γ . Spontaneous symmetry breaking and the process by which gauge bosons
¹⁹⁵ acquire mass will be addressed in section 1.3.1.

¹⁹⁶ Noether's theorem [4] stipulates that any continuous symmetry is associated with a conserved
¹⁹⁷ quantity. In the Standard Model, this means that the $SU(3)_C$ symmetry gives rise to conservation of
¹⁹⁸ color charge. The $SU(2)_L \times U(1)_Y$ symmetry gives rise to conservation of electromagnetic charge.
¹⁹⁹ Conservation of spin results from the Poincaré symmetry described by the theory of special rela-
²⁰⁰ tivity, which combined with Noether's theorem gives us the conversation of energy, momentum,
²⁰¹ and angular momentum.

²⁰² The SM Lagrangian is invariant under CPT symmetry, or charge, parity, and time reversal.
²⁰³ Charge conjugation (C) transform a particle into it's corresponding antiparticle by reversing the
²⁰⁴ charge and other quantum numbers. Parity conjugation (P) reverses spatial coordinates, which
²⁰⁵ transforms left-handed particles into right-handed particles and vice-versa. Time reversal (T) is
²⁰⁶ the theoretical process of reversing time. The L subscript in the $SU(2)_L$ group indicates that this
²⁰⁷ symmetry only applies to left-handed fermions. As a result, the $W^{1,2,3}$ gauge bosons of $SU(2)_L$

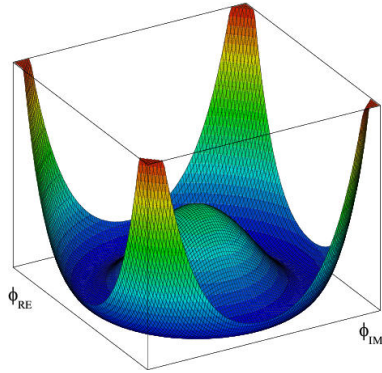


Figure 1.4: An illustration of the “hat shaped” potential of the Higgs field, resulting in a non-zero vacuum expectation value.

only interact with left handed particles, a process which maximally violates P-symmetry in the weak force. A small amount of the CP symmetry violation is also observed in the Standard Model, through the decays of strange flavored mesons [5]. The CPT theorem posits that the violation of CP symmetry implies that T-symmetry must also be violated, so that CPT is a preserved symmetry.

1.3.1 Spontaneous Symmetry Breaking and The Higgs Mechanism

Spontaneous symmetry breaking is the process by which a Lagrangian obeys a symmetry at high energies, but exhibits asymmetric behavior at lower energies. The electroweak symmetry group is spontaneously broken as $SU(2)_L \times U(1)_Y \rightarrow U(1)_{EM}$. The quantity conserved by the $SU(2)_L$ symmetry is weak isospin $T_{1,2,3}$, while the quantity conserved by $U(1)_Y$ symmetry is weak hypercharge Y . Below very high energies, the presence of the Higgs field causes the electroweak symmetry to break. The Higgs field is scalar field which forms a complex doublet of the $SU(2)$ symmetry group, with four degrees of freedom. The shape of the Higgs field potential, shown in Figure 1.4, results in a ground state with a non-zero vacuum expectation value; thus the Higgs field takes a non-zero value throughout all space, which breaks the symmetry of the weak isospin $SU(2)$ group.

The interaction with the Higgs field mixes the four massless gauge bosons $W^{1,2,3}$ and B . Three Higgs field degrees of freedom mix with the massless gauge bosons, resulting in three massive gauge bosons W^- , W^+ and Z^0 . The massless photon γ is created from the components of the

226 massless gauge bosons which do not interact with the Higgs field. The scalar Higgs boson arises
227 from the one unmixed degree of freedom the Higgs field. Spontaneous symmetry breaking also
228 violates the conservation of weak isospin and weak hypercharge, leaving only electromagnetic
229 charge ($Q = T_3 + \frac{1}{2}Y$) as a conserved quantity associated with the $U(1)_{EM}$ symmetry.

230 **1.4 Experimental Validation of the Standard Model**

231 The theoretical framework of the Standard Model coalesced into a unified theory in the mid-
232 20th century. A cascade of discoveries providing empirical evidence for the model followed
233 closely. In the 1960s, three quarks (up, down and strange) and four leptons (electron, muon,
234 and their associated neutrinos) were the known particulate building blocks of matter and the Stan-
235 dard Model. The discovery of the charm quark in 1974, through the observation of the J/ψ meson
236 [6][7], confirmed the existence of a fourth quark flavor. The discovery of the τ in 1975 [8] provided
237 the first evidence of a 3rd generation of matter. This was quickly followed by the observation of
238 the Υ meson in 1977 [9], which provided evidence for the existence of a fifth quark, the b quark
239 (bottom, or beauty). The existence of a 3rd generation of fermion also explained the observation
240 of CP violation in the weak force, as it allowed for the addition of a complex phase in the CKM
241 matrix (a unitary matrix which describes flavor mixing in the weak interaction). The top quark
242 (t) and tau neutrino (ν_τ) were predicted at this point as the final building blocks of three complete
243 generations of fermions, and they were discovered by experimental observation around the turn of
244 the 21st century [10] [11] [12].

245 The W and Z bosons were predicted by the Standard Model, but to observe them required the
246 construction of a particle accelerator powerful enough to produce them. They were finally observed
247 at CERN in 1983 by the UA1 and UA2 experiments [13] [14] at the newly constructed Super Proton
248 Synchrotron (SPS). Their masses were observed to be compatible with the masses predicted by the
249 Standard Model nearly a decade earlier. The final missing piece then was confirming the existence
250 of the Higgs, which again required the construction of a newer and more powerful collider. CERN
251 achieved this with the construction of the Large Hadron Collider (LHC), and in 2012 the ATLAS

252 and CMS experiments announced the discovery of the Higgs particle [15] [16].

253 **1.5 Limitations of the Standard Model**

254 While the Standard Model has enjoyed decades of experimental results which confirm its pre-
255 dictions, there are several glaring shortcomings. The observed phenomenon for which the Standard
256 Model provides no explanation are summarized below.

- 257 • Gravity - the Standard Model does not account for the fourth fundamental force of gravity.
- 258 • Dark Matter - there is no viable candidate to explain the existence of dark matter, a non-
259 interacting form of matter which must exist to account for gravitational observations which
260 cannot be explained by general relativity, such as the motion of galaxies, gravitational lens-
261 ing, and the structure of the universe [17].
- 262 • Matter-Antimatter asymmetry - the level of CP violation in the Standard Model isn't suf-
263 ficient to explain the large discrepancy between the amount of matter and the amount of
264 antimatter in the universe today, and the origins of this imbalance are not understood.
- 265 • Neutrino masses - the Standard Model assumes that neutrinos are massless and provides
266 no mechanism for them to acquire mass. However, observations of neutrino oscillations
267 indicates they posses some small non-zero mass [18].

268 In addition to these unexplained natural phenomenon, there are several questions about the
269 *naturalness* of the Standard Model. The principle of naturalness states that dimensionless ratios
270 between physical constants should be of order 1, and that nature should not be arbitrarily fine-
271 tuned. While this is largely an aesthetic argument, it points to many aspects of the Standard Model
272 for which there exists no natural explanation.

- 273 • Strong CP - while CP symmetry is violated in the weak force, observations indicate that it
274 is preserved by the strong force [19]. The Standard Model predicts that CP violation in the

275 strong force is possible. There is no principle which motivates this incongruity between the
276 weak force and strong force.

- 277 • Hierarchy Problem - The wide range of masses for elementary particles and the wide range of
278 scales at which the four fundamental forces operate is not motivated by the SM. Specifically,
279 it is not understood why the Higgs mass is observed to be well below the Plank scale λ ,
280 which is the energy level at which the effects of quantum gravity become significant. QFT
281 indicates that the Higgs mass is determined by contributions from all energy scales including
282 λ , meaning that its observed mass is inexplicably small.

283 The limitations of the Standard Model provide a road map for theoretical and experimental
284 particle physicists, who seek to develop new theories which account for these observations, and
285 then to find evidence which might support these *Beyond the Standard Model* (BSM) theories. The
286 next chapter will introduce the BSM theories which motivate the physics search presented in this
287 thesis.

Chapter 2: Physics Beyond the Standard Model

290 In light of the various phenomenon unexplained by the Standard Model, physicists have pro-
 291 posed various extensions to the Standard Model, collectively termed *Beyond the Standard Model*
 292 (BSM) theories. A particular focus of the physic programs at the Large Hadron Collider (LHC) are
 293 BSM models which suggest dark matter candidate particles. If these particles couple to Standard
 294 Model, they could be produced and observed at the LHC.

295 **2.1 Hidden Valley Models**

296 Hidden Valley (HV) models are a category of BSM models that allow for dark matter (DM)
 297 production at the LHC. They extend the Standard Model with an additional non-Abelian gauge
 298 group [20]. This introduces the possibility of a complex dark sector, which mirrors the complexities
 299 of Standard Model QCD, and introduces the possibility of dark quarks and gluons. The term
 300 “hidden valley” refers to the idea that the DM is hidden from the SM by a high-energy barrier, as
 301 illustrated in Figure ???. The dark sector is assumed to communicate with the Standard Model via
 302 a “portal”, or “messenger particle”, that can interact with both Standard Model and HV forces. For
 303 the s-channel scenario, the portal is considered to be a new massive mediator particle Z' .

304 The portal particle allows for the production of dark sector particles at hadron colliders. If
 305 dark quarks are produced via the decay $Z' \rightarrow q_D q_D$ they can hadronize and form dark jets. The
 306 properties of the dark jets are determined by the dynamics of the dark sector, which are explored in
 307 the subsequent section. Depending on the details of the model, the jets formed by the dark hadrons
 308 can be categorized as fully dark, semi-visible, leptonic, emerging, or other [20].

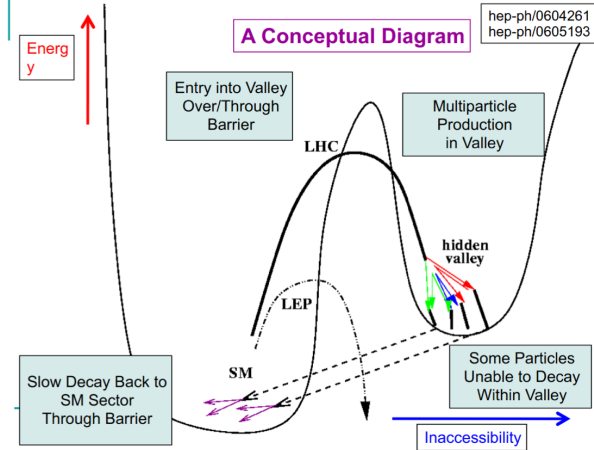


Figure 2.1: Illustration of the hidden valley potential

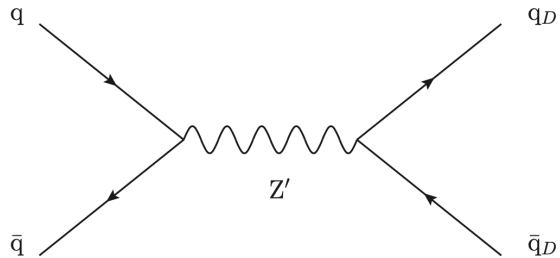


Figure 2.2: The massive mediator particle Z' of the s-channel realization of a HV model

309 2.2 Dark QCD

310 The theoretical underpinning of the semi-visible jet phenomenology is a dark sector with a
 311 gauge group $SU(N_d)$ leading to confinement at a scale Λ_d . For illustration, let's consider the
 312 case of an $SU(2)_d$ gauge theory, which gives rise to two dark fermionic generations $\chi_a = \chi_1, \chi_2$.
 313 Following the work of Timothy Cohen, et.al. we can write the fundamental dark Lagrangian as:

$$\mathcal{L}_{dark} \supset -\frac{1}{2} \text{Tr } G_{\mu\nu}^d G^{d\mu\nu} - \bar{\chi}_a (i \not{D} - M_{d,a}) \chi_a \quad (2.1)$$

314 The first term allows for the dark gluons to self-interact, while the second term enables the dark
 315 quarks to hadronize and acquire mass. The dark quarks are assumed to have a common mass M_d .
 316 The coupling strength of the strongly interacting dark quarks is termed α_d . At the confinement

317 scale Λ_d , the dark quarks can form bound states. At the scale $M_d \approx \Lambda_d$ a QCD-like show occurs.

318 The properties of the hadrons formed by the dark quarks are of particular importance to the
319 observed dark QCD dynamics. Dark-isospin number $U(1)_{1-2}$ and dark-baryon number $U(1)_{1+2}$
320 are accidental symmetries of the theory which determine the stability of the hadrons. In the case
321 of two dark flavors, six dark hadrons can be formed: four mesons ($\chi_1\bar{\chi}_1$, $\chi_2\bar{\chi}_2$, $\chi_1\bar{\chi}_2$, $\bar{\chi}_1\chi_2$) and
322 two baryons ($\bar{\chi}_1\bar{\chi}_2$, $\bar{\chi}_1\bar{\chi}_2$). The mesons $\chi_1\bar{\chi}_2$ and $\bar{\chi}_1\chi_2$ are charged under dark-isospin and will be
323 stable if this symmetry is unbroken. The baryons would also be stable as they are charged under
324 the dark-baryon number. These four stable hadrons become dark matter candidates of the theory.
325 The $\chi_1\bar{\chi}_1$ and $\chi_2\bar{\chi}_2$ mesons are not charged under either symmetry and are thus expected to decay.
326 The unstable mesons can decay into stable dark mesons, or into an off-shell Z' . The off-shell Z'
327 will then decay into two DM quarks or two SM quarks, and its products will continue to shower
328 until the final state particles are stable.

329 The number of stable and unstable dark states varies substantially depending on the details
330 of the model. The model discussed above can be generalized from $SU(2)_d$ to $SU(N)_d$, with any
331 number of colors N_c or flavors N_f . This affects the ratio of possible stable to unstable mesons,
332 which can directly impact the amount of missing energy. The fraction of missing energy is a
333 variable in many dark QCD models, and is especially important in the case of semi-visible jets.

334 2.3 Semi-visible Jets

335 A “semi-visible jet” occurs when the heavy Z' messenger particle decays into dark quarks,
336 which then hadronize in a QCD-like shower. If some of the dark hadrons are stable while others
337 decay to SM quarks via the off-shell Z' , a collimated mixture of visible and dark matter is formed
338 – this is termed a semi-visible jet. If the Z' messenger particle is produced at rest, the two jets will
339 be back-to-back in the transverse plane. If there is an imbalance in the amount of invisible particles
340 between the two jets, one of the jets will be observed to be aligned with missing transverse energy.

341 While there are a myriad of HV and dark QCD models, a handful of model parameters are most
342 important in determining the observable of these showers within a particle detector. The coupling

343 strength α_d is one of the most important, as it controls the fraction of dark hadrons emitted in the
344 shower and their average p_T . The mass of the dark quarks directly impacts the jet mass. If the
345 masses of the dark quark flavors are comparable, the ratio of stable to unstable dark hadrons will
346 be approximately 1:1. However, if there is a mass splitting, stable or unstable dark hadrons may
347 be favored, which impacts the amount of missing energy observed.

348 The ratio of stable to unstable dark hadrons in the shower is a critical variable for capturing the
349 behavior of dark showers. This value is termed r_{inv} :

$$r_{inv} = \frac{\# \text{ of stable hadrons}}{\# \text{ of hadrons}} \quad (2.2)$$

350 Events containing jets aligned with missing transverse momentum are generally considered to
351 be misreconstructed by other DM searches, and therefore discarded. This class of final states is
352 therefore largely uncovered by existing DM searches. The nature of the dark hadron shower is
353 determined by the following parameters: the Z' mass $m_{Z'}$, the Z' couplings to visible and dark
354 quarks g_q and g_{q_D} , the number of dark colors and flavors, the characteristic scale of the dark sector
355 confinement Λ_D , the scale of the dark hadrons m_D , and the average fraction of stable hadrons in
356 the decay r_{inv} . The coupling to SM quarks determines the Z' production cross section.

357

358

Chapter 3: The Large Hadron Collider

359 The Large Hadron Collider (LHC) is a 26.7 km circular high-energy particle accelerator, span-
360 ning the Swiss-French border near the city of Geneva, Switzerland [21]. The LHC occupies the
361 tunnel constructed in 1989 for the Large Electron-Positron (LEP) Collider, and reaches a maxi-
362 mum depth of 170m below the surface. The LHC is operated by the European Organization for
363 Nuclear Research (CERN), the largest international scientific collaboration in the world.

364 The LHC accelerates protons and heavy ions, and collides them at four interaction points
365 around the ring, with a design center-of-mass energy per collision of $\sqrt{s} = 14$ TeV. Each interaction
366 point is home to one of four detector experiments, which study the products of the collisions. The
367 largest of these experiments is the ATLAS detector, a general purpose detector designed to study
368 the Standard Model and search for new physics that could be produced in LHC collisions [22].
369 The CMS detector is another general purpose detector, designed and operated independently of the
370 ATLAS detector, but intended to probe the same range of physics [23]. The ALICE experiment is
371 a dedicated heavy ion experiment, and the LHC-b experiment is a dedicated *b*-physics experiment
372 [24] [25].

373 This chapter will cover the multi-component accelerator complex powering the LHC, the state-
374 of-the-art magnets which steer the particle beams, measurements of the intensity and number of
375 collisions produced by the LHC, and finally an overview of LHC activities in the past, present, and
376 future.

³⁷⁷ **3.1 Accelerator Physics**

³⁷⁸ **3.1.1 The Journey of a Proton**

³⁷⁹ From 2010 - 2018, the protons which fed the LHC started as hydrogen gas. The electrons were
³⁸⁰ removed from the hydrogen atoms through the use of strong electric fields. The linear accelerator
³⁸¹ LINAC2 then accelerated the protons to an energy of 50 MeV. Between 2018 and 2020, LINAC2
³⁸² was replaced with LINAC4, which instead accelerates H^- ions, hydrogen atoms with two electrons.
³⁸³ LINAC4 is capable of accelerating the H^- ions to 160 MeV. Before injection to the next part of
³⁸⁴ the acceleration chain, both electrons are stripped from the H^- ions, leaving just protons. From
³⁸⁵ here the protons enter the Proton Synchrotron booster, where they are accelerated up to 1.4 GeV of
³⁸⁶ energy. Subsequently they are sorted into bunches separated in time by 25 ns, where each bunch
³⁸⁷ contains approximately 10^{11} protons. Next the bunches pass through the Proton Synchrotron (PS)
³⁸⁸ and the Super Proton Synchrotron (SPS), where they reach energies of 25 GeV and 450 GeV
³⁸⁹ respectively. Finally they are injected into the LHC as two beams traveling in opposite direction.
³⁹⁰ The original design allowed each beam to be accelerated up to 7 TeV of energy. Due to limitations
³⁹¹ in the performance of the superconducting LHC magnets, the highest energy actually achieved by
³⁹² the LHC beams during Run 2 was 6.5 TeV, giving a collision center-of-mass energy of $\sqrt{s} = 13$
³⁹³ TeV [26]. Figure 3.1 shows the full LHC accelerator complex.

³⁹⁴ Acceleration in the LHC is performed by eight radio frequency (RF) cavities located around the
³⁹⁵ ring. Each RF cavity produces a 2 MV electric field oscillating at 40 MHz. The 40MHz oscillation
³⁹⁶ produces a point of stable equilibrium every 2.5 ns. These points of equilibrium are synchronized
³⁹⁷ with the occurrence of the proton bunches produced in the PS – a proton bunch occupies one out
³⁹⁸ of every ten points of stable equilibrium, such that the bunches maintain a 25 ns spacing [26].

³⁹⁹

The CERN accelerator complex Complexe des accélérateurs du CERN

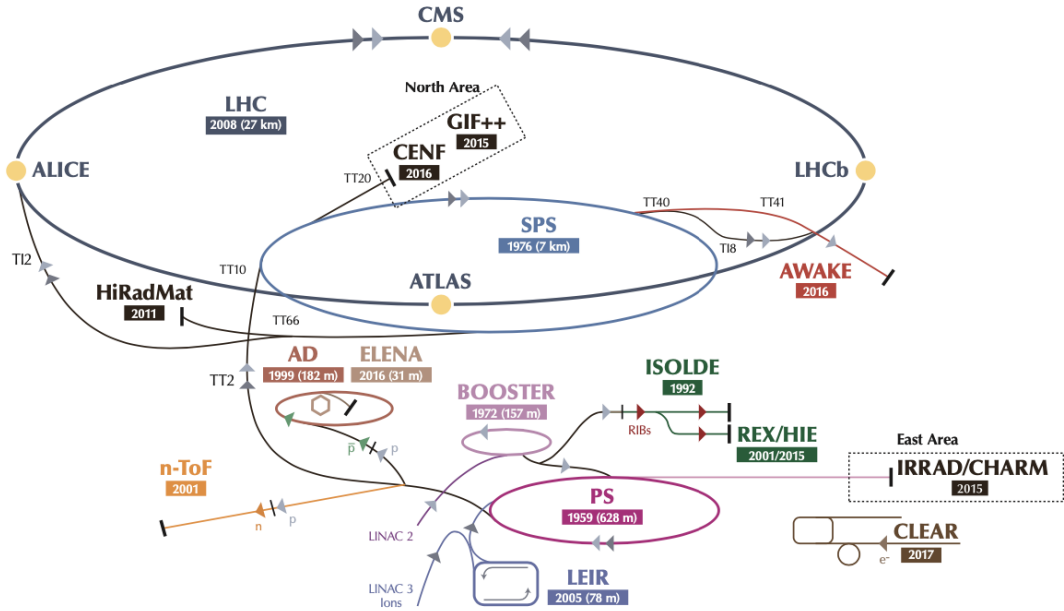


Figure 3.1: The LHC accelerator complex at CERN [27]

400 3.1.2 Magnets

401 In addition to the acceleration cavities, the LHC houses 9593 superconducting magnets which
 402 direct and focus the proton beam on its 27 kilometer journey. The magnets are comprised of super-
 403 conducting Niobium-Titanium coils cooled to 1.9K by superfluid helium. As the beams approach
 404 one of the four collision points around the ring, multipole magnets focus and squeeze the beam for
 405 optimal collisions [26].

406 The LHC is divided into sections, where each section contains an arc and a straight insertion. The arcs are composed of 1232 large dipole magnets which bend the beam
 407 to follow the roughly circular 27 km path. The main dipoles generate powerful 8.3 tesla magnetic
 408 fields to achieve this bend. Each dipole magnet is 15 meters long and weighs 35 tonnes. The
 409 dipoles work in conjunction with quadrupole magnets, which keep the particles in a focused beam,
 410 and smaller sextupole, octupole and decapole magnets which tune the magnetic field at the ends of
 411 the dipole magnets [28].

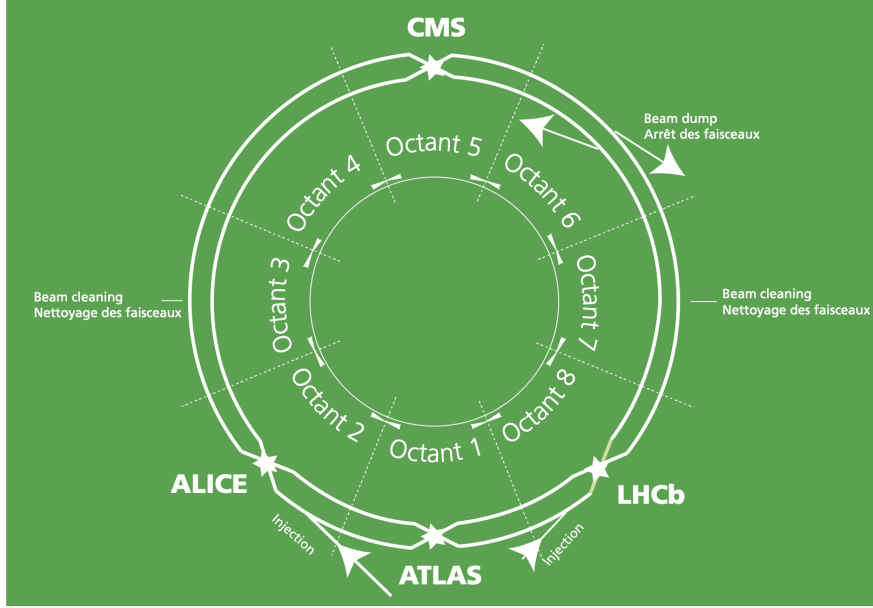


Figure 3.2: The octants of the LHC and location of various beam activities [26]. Stars indicate the locations of beam collisions, and the associated detectors recording the outcome of those collisions.

413 The straight insertion sections have different purposes depending on their location around the
 414 ring: beam collisions, beam injection, beam dumping, or beam cleaning. At the four collision
 415 points, insertion magnets squeeze the beam to ensure a highly focused collision. This is accom-
 416 plished with a triplet of quadrupole magnets, which tighten the beam from 0.2 millimeters to just
 417 16 micrometers in diameter. Insertion magnets also clean the beam, which prevents stray particles
 418 from hitting sensitive components throughout the LHC. When the LHC is ready to dispose of a
 419 beam of particles, beam dump magnets deflect the path of the beam into a straight line towards
 420 a block of concrete and graphite that stops the beam. A dilution magnet then reduces the beam
 421 intensity by a factor of 100,000 before the final stop [28]. Figure 3.2 shows the locations various
 422 beam activities.

423 3.2 Luminosity

424 Collisions at the LHC occur when the two beams of proton bunches cross at one of the four
 425 interaction points. The intensity of collisions is described by the instantaneous luminosity, the

426 formula for which is given in equation 3.1.

$$L = \frac{fN_1N_2}{4\pi\sigma_x\sigma_y} \quad (3.1)$$

427 Here f is the revolution frequency, N_1 and N_2 are the number of particle per bunch for each
428 beam, and σ_x , σ_y are the horizontal and vertical beam widths.

429 The instantaneous luminosity gives the number of the collisions that could be produced at the
430 interaction point per unit of cross-sectional area per unit of time, generally expressed in $\text{cm}^{-2}\text{s}^{-1}$.
431 The integrated luminosity is obtained by integrating the instantaneous luminosity over a given
432 block of time, and measures the total number of collisions which have occurred during that op-
433 eration period. The total integrated luminosity is directly correlated with the size of the datasets
434 collected by the LHC experiments. Total integrated luminosity for Run 2 is illustrated in Figure
435 3.3.

436 High levels of instantaneous luminosity result in multiple pp collisions per bunch crossing,
437 which leads to an effect known as *pileup*. Pileup poses a challenge for detector physics, as recon-
438 structing the products of multiple simultaneous events is far more challenging than reconstructing
439 a single event with no pileup. Pileup conditions vary from year-to-year and run-to-run of LHC op-
440 eration, and the impact of these conditions are taken into account when analyzing the data, as will
441 be discussed further in Chapter 5. Measurement of pileup conditions during Run 2 are illustrated
442 in Figure 3.3.

443 The design peak luminosity of the LHC is $1.0 \times 10^{34} \text{ cm}^{-2}\text{s}^{-1}$. During Run 1 of the LHC the
444 peak instantaneous luminosity was $0.8 \times 10^{34} \text{ cm}^{-2}\text{s}^{-1}$. Over the course of Run 1 the LHC collected
445 a total integrated luminosity of 5.46 fb^{-1} at $\sqrt{s} = 7 \text{ TeV}$, and 22.8 fb^{-1} at $\sqrt{s} = 8 \text{ TeV}$. Following the
446 first long shutdown and upgrade phase of operations, the LHC achieved a center of mass energy
447 $\sqrt{s} = 13 \text{ TeV}$ at the beginning of Run 2 in 2015. The LHC was also able to deliver 2.0×10^{34}
448 $\text{cm}^{-2}\text{s}^{-1}$ peak instantaneous luminosity, double the design value. During LHC Run 2, from 2015-
449 2018, the LHC delivered 156 fb^{-1} of integrated luminosity for proton-proton collisions. Run 3 of

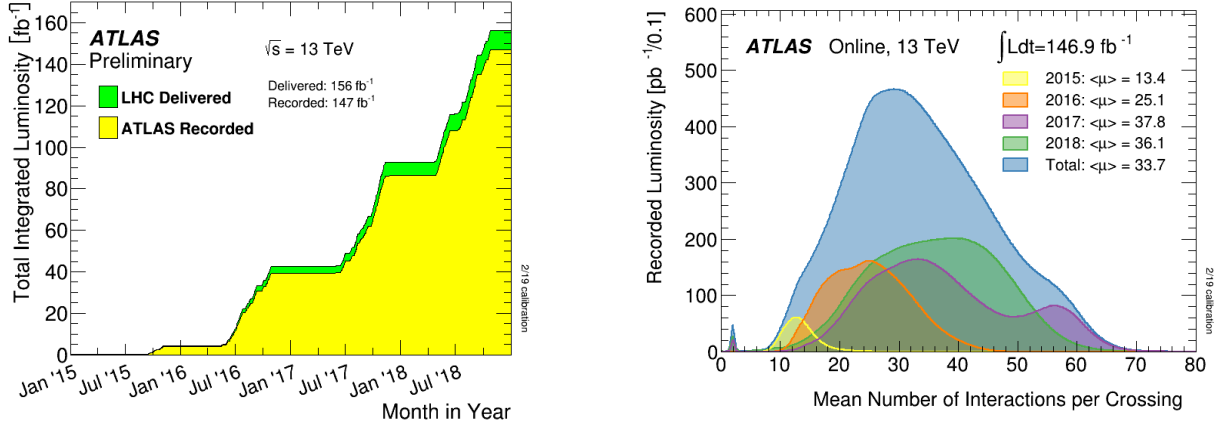


Figure 3.3: (Left) Total integrated luminosity over the course of Run 2. (Right) Average number of pp interactions per bunch crossing in Run 2. Each curve is weighted by the integrated luminosity for the year.

450 the LHC began in 2022, and is expected to deliver 250 fb^{-1} of integrated luminosity to the ATLAS
451 and CMS experiments by 2026 [29].

452 The goal of LHC physic analyses is to find and study rare events produced by interesting
453 physics processes. The cross section σ of a given process indicates the probability of that process
454 occurring given the beam conditions of the LHC. Multiplying the cross section by the integrated
455 luminosity of a dataset gives the expected number of events for that process within the dataset.

$$N_{\text{events}} = \int \sigma L(t) dt = \mathcal{L} \times \sigma \quad (3.2)$$

456 The cross section for most processes of interest, especially BSM processes, is several orders of
457 magnitude below the total cross section for the LHC. Therefore maximizing the number of events
458 produced in collisions is crucial to increase the likelihood of producing events from processes of
459 interest. For this reason, maximizing instantaneous luminosity is a key factor in accelerator design
460 and operation, while mitigating the resulting pileup effects is a key component in detector design
461 and operation.

462 **3.3 LHC Timeline**

463 The first proton-proton collisions at the LHC were achieved in 2010 with a center-of-mass
464 energy of $\sqrt{s} = 7$ TeV. Run 1 of the LHC took place between 2010 and early 2013, during which
465 time the center-of-mass collision energy increased from 7 TeV to 8 TeV. Figure 3.4 shows an
466 overview of LHC activities beginning in 2011, in the midst of Run 1. The data collected during
467 Run 1 led to the discovery of the Higgs Boston in 2012 [30].

468 Between 2013 and 2015 the LHC underwent the first Long Shutdown (LS1) during which
469 time maintenance and renovation was performed on the accelerator chain, including the repair and
470 consolidation of the high-current splices which connect the super-conducting LHC magnets. Run
471 2 of the LHC took place from 2015 to 2018 and achieved a center-of-mass energy of $\sqrt{s} = 13$ TeV.
472 Analysis of data collected in Run 2 is still on going, and is the subject of study in this thesis.

473 Between 2018 and 2022 the LHC underwent the second Long Shutdown (LS2), allowing for
474 further detector and accelerator maintenance and upgrades. Key improvements to the LHC in-
475 cluded the improvement of the insulation for over 1200 diode magnets, and the upgrade from
476 LINAC2 to LINAC4 mentioned in Section 3.1.1. Run 3 of the LHC began in 2022 and achieved a
477 center-of-mass energy of $\sqrt{s} = 13.6$ TeV.

478 Run 3 is scheduled to continue through 2026, at which point the LHC machine and detectors
479 will undergo upgrades for the *high luminosity* LHC (HL-LHC). The HL-LHC will increase the
480 instantaneous machine luminosity by a factor of 5 - 7.5 with respect to the nominal LHC design.
481 The bottom panel of Figure 3.4 shows an overview of the preparation work for the HL-LHC that
482 has been going on concurrently with Run 1, 2, and 3 of the LHC [31].



Figure 3.4: Timeline of LHC and HL-LHC activities [29]. Integrated luminosity estimates are approximate, and not reflective of the exact amount delivered to each experiment.

483

484

Chapter 4: The ATLAS Detector

485 The ATLAS detector (**A** Toroidal **L**H**C** Apparatu**S**) is one of two general purpose physics
486 detectors designed to study the products of proton-proton collisions at the LHC. The detector is
487 composed of a variety of specialized subsystems, designed to fully capture a wide array of physics
488 processes. The apparatus is 25m high, 44m in length, and weighs over 7000 tons [32]. The LHC
489 beam pipes direct proton beams to an interaction point at the center of ATLAS, and the cylindrical
490 detector design captures a complete 360° view of the *event*, tracking all particles that result from
491 the collision.

492 The main components of the ATLAS detector are the Inner Detector (ID) which provides high
493 precision tracking of charged particles leaving the collision vertex, the calorimeter system which
494 measures the energy of electromagnetic and hadronic objects, and the Muon Spectrometer (MS)
495 which gives detailed information about muons that reach the outer radii of the detector. Two
496 magnet systems, a 2 T solenoid magnet surrounding the ID, and a 0.5-1.0 T toroid magnet system
497 situated throughout the MS, produce magnetic fields which bend the trajectory of charged particles
498 traversing the detector. In addition to the main detector components, dedicated forward detectors
499 monitor beam conditions and instantaneous luminosity, and an online trigger system reduces the
500 data rate to a manageable level for storage. Each of these components will be discussed in further
501 detail in this chapter.

502 **4.1 Coordinate System and Geometry**

503 The ATLAS detector employs a right hand cylindrical coordinate system. The z axis is aligned
504 with the beam line, and the x-y plane sits perpendicular to the beam line. The coordinate system
505 origin is centered on the detector, such that the origin corresponds with the interaction point of the

506 two colliding beams. The detector geometry is usually characterized by polar coordinates, where
507 the azimuthal angle ϕ spans the x-y plane. The polar angle θ represents the angle away from the
508 beam line, or z axis. $\theta = 0$ aligns with the positive z -axis, and $\phi = 0$ aligns with the positive x-axis.

509 The polar coordinate θ is generally replaced by the Lorentz invariant quantity *rapidity* or y :

$$y = \frac{1}{2} \ln\left(\frac{E + p_z}{E - p_z}\right). \quad (4.1)$$

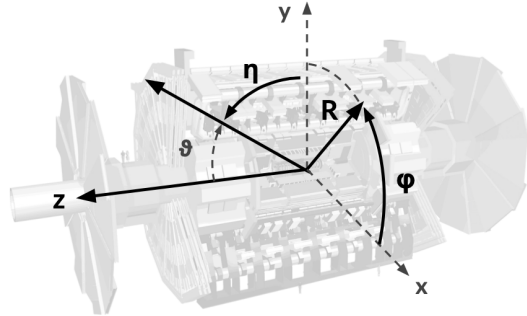
510 This substitution is advantageous because objects in the detector are traveling at highly rela-
511 tivistic speeds. The relativistic speed also means that the masses of the particles are generally small
512 compared to their total energy. In the limit of zero mass, the rapidity y reduces to the pseudorapid-
513 ity η , which can be calculated directly from the polar angle θ :

$$\eta = -\ln\left(\frac{\theta}{2}\right). \quad (4.2)$$

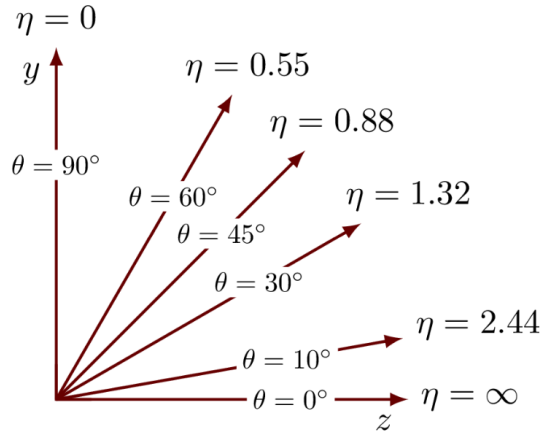
514 The distance between physics objects in the detector is generally expressed in terms of the solid
515 angle between them ΔR :

$$\Delta R = \sqrt{\Delta\phi^2 + \Delta\eta^2} \quad (4.3)$$

516 Figure 4.1a depicts the orientation of the coordinate system with respect to the ATLAS detector,
517 while Figure 4.1b illustrates the relationship between θ , η , and the beamline axis z . Direct or “head
518 on” proton-proton collisions are more likely to result in objects whose momentum is directed
519 along transverse plane (low $|\eta|$); glancing proton-proton collisions are more likely to result in
520 objects whose momentum is directed along the z -axis (high $|\eta|$). Due to the difference in the
521 nature of these collisions, as well as the cylindrical design of the ATLAS detector, the detector
522 is divided into regions of low and high η . Each subsystem has a “central” or “barrel” region
523 covering low $|\eta|$, while the “forward” or “end-cap” regions cover the area up to $|\eta| = 4.9$. Each of
524 the three main ATLAS subsystems will be discussed in the following sections.



(a) The ATLAS geometry



(b) Relationship between η and θ

Figure 4.1: ATLAS coordinate system and geometry

525 4.2 Inner Detector

526 The Inner Detector (ID) is the ATLAS subsystem closest to the interaction point. The primary
 527 purpose of the ID is to determine the charge, momentum, and trajectory of charged particles pass-
 528 ing through the detector. With this information the ID is also able to precisely determine interaction
 529 vertices.

530 The ID is composed of three sub-detectors; the Pixel Detector, the Semiconductor Tracker
 531 (SCT) and the Transition Radiation Tracker (TRT). Figure 4.2 shows the location of these three
 532 subsystems with respect to each other and the interaction point.

533 4.2.1 Pixel Detector

534 The pixel detector is the first detector encountered by particles produced in LHC collisions.
 535 The original pixel detector consists of 3 barrel layers of silicon pixels, positioned at 5 cm, 9 cm
 536 and 12 cm from the beamline. There are also 3 disks on each end-cap positioned 50 - 65 cm from
 537 the interaction point, providing full coverage for $|\eta| < 2.2$. The layers are comprised of silicon
 538 pixels each measuring $50 \times 400 \mu\text{m}^2$, with 140 million pixels in total. The pixels are organized
 539 into modules, which each contain a set of radiation hard readout electronics chips. In 2014, the
 540 Insertable B-layer (IBL) was installed, creating a new innermost layer of the pixel detector sitting

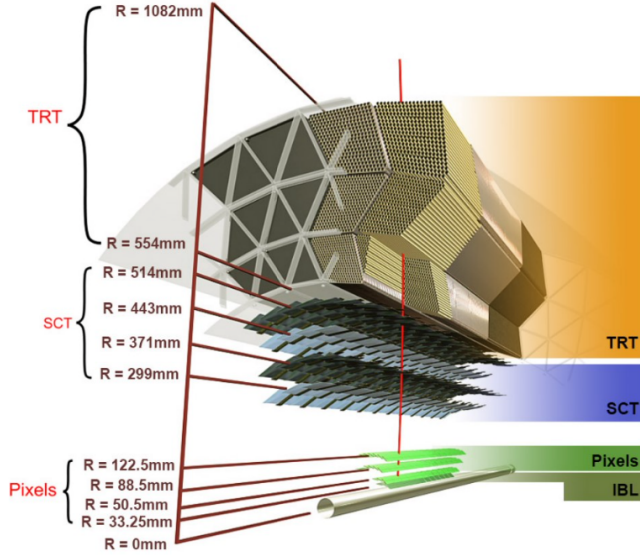


Figure 4.2: A 3D visualization of the structure of the ID in the barrel region [33]

541 just 3.3 cm from the beamline. The pixels of the IBL measure $50 \mu\text{m}$ by $250 \mu\text{m}$, and cover
 542 a pseudo-rapidity range up to $|\eta| < 3$. The IBL upgrade enhances the pixel detector's ability
 543 to reconstruct secondary vertices associated with short-lived particles such as the b-quark. The
 544 improved vertex identification also helped compensate for increasing pile-up in Run 2 [32].

545 4.2.2 Semiconductor Tracker

546 The SCT provides at least 4 additional measurements of each charged particle. It employs the
 547 same silicon technology as the Pixel Detector, but utilizes larger silicon strips which measure $80 \mu\text{m}$
 548 by 12.4 cm . The SCT is composed of 4 barrel layers, located between 30 cm and 52 cm from
 549 the beamline, and 9 end-cap layers on each side. The SCT can distinguish tracks that are separated
 550 by at least $200 \mu\text{m}$.

551 4.2.3 Transition Radiation Tracker

552 The TRT provides an additional 36 hits per particle track. The detector relies on gas filled
 553 straw tubes, a technology which is intrinsically radiation hard. The straws which are each 4 mm in
 554 diameter and up to 150 cm in length and filled with xenon gas. The detector is composed of about

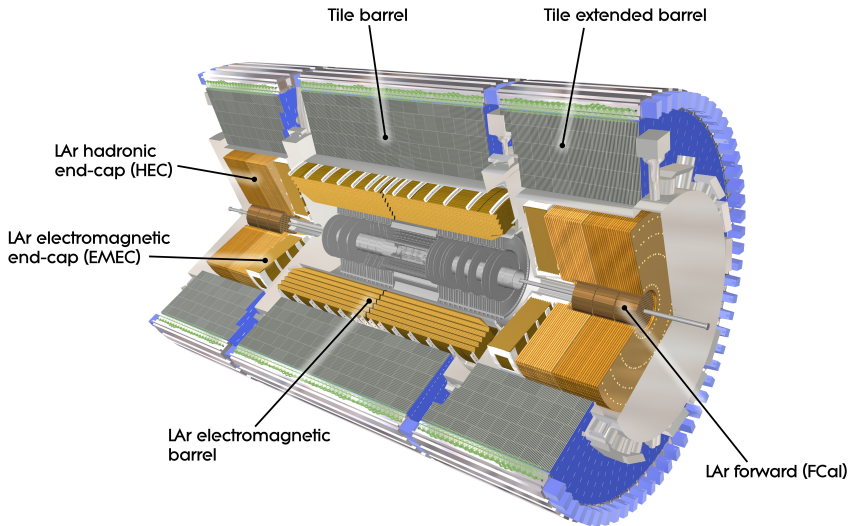


Figure 4.3: ATLAS calorimetry system [34]

555 50000 barrel region straws and 640000 end-cap straws, comprising 420000 electronic readout
 556 channels. Each channel provides a drift time measurement with a spatial resolution of $170\ \mu\text{m}$ per
 557 straw. As charged particles pass through the many layers of the detector, transition radiation is
 558 emitted. The use of two different drift time thresholds allows the detector to distinguish between
 559 tracking hits and transition radiation hits.

560 4.3 Calorimeters

561 The ATLAS calorimeter system is responsible for measuring the energy of electromagnetically
 562 interacting and hadronically interacting particles passing through the detector. The calorimeters are
 563 located just outside the central solenoid magnet, which encloses the inner detectors. The calorime-
 564 ters also stop most known particles, which the exception of muons and neutrinos, preventing them
 565 from traveling to the outermost layers of the detector. The ATLAS calorimetry system is composed
 566 of two subsystems - the Liquid Argon (LAr) calorimeter for electromagnetic calorimetry and the
 567 Tile calorimeter for hadronic calorimetry. The full calorimetry system is shown in Figure 4.3.

568 4.3.1 Liquid Argon Calorimeter

569 The LAr calorimeter is a sampling calorimeter designed to trigger on and measure the ener-
570 gies of electromagnetic (EM) particles, as well as hadronic particles in the high η regions. It is
571 divided in several regions, as shown in Figure 4.3. For the region $|\eta| < 1.4$, the electromagnetic
572 barrel (EMB) is responsible for EM calorimetry, and provides high resolution energy, timing,
573 and position measurements for electrons and photons passing through the detector. The elec-
574 tromagnetic endcap (EMEC) provides additional EM calorimetry up to $|\eta| < 3.2$. In the re-
575 gion $1.4 < |\eta| < 3.2$, the hadronic endcap (HEC) provides hadronic calorimetry. For hadronic
576 calorimetry in the region $|\eta| < 1.4$, corresponding to a detector radii > 2.2 m, the less expensive
577 tile calorimeter (discussed in the next section) is used instead. A forward calorimeter (FCAL)
578 extends the hadronic calorimetry coverage up to $3.1 < |\eta| < 4.8$ [35].

579 The LAr calorimeter is composed of liquid argon sandwiched between layers of absorber mate-
580 rial and electrodes. Liquid argon is advantageous as a calorimeter active medium due to its natural
581 abundance and low cost, chemical stability, radiation tolerance, and linear response over a large
582 energy range [36]. The calorimeter is cooled to 87k by three cryostats: one barrel cryostat encom-
583 passing the EMB, and two endcap cryostats. The barrel cryostat also encloses the solenoid which
584 produces the 2T magnetic field for the inner detector. Front-end electronics are housed outside the
585 cryostats and are used to process, temporarily store, and transfer the calorimeter signals.

586 **Electromagnetic Calorimeter**

587 For the electromagnetic calorimeters, the layers of electrodes and absorber materials are ar-
588 ranged in an an accordion shape, as illustrated in Figure 4.4. The accordion shape ensures that
589 each half barrel is continuous in the azimuthal angle, which is a key feature for ensuring consistent
590 high resolution measurements. Liquid argon permeates the space between the lead absorber plates,
591 and a multilayer copper-polymide readout board runs through the center of the liquid argon filled
592 gap.

593 The detection principle for the LAr calorimeter is the current created by electrons which are

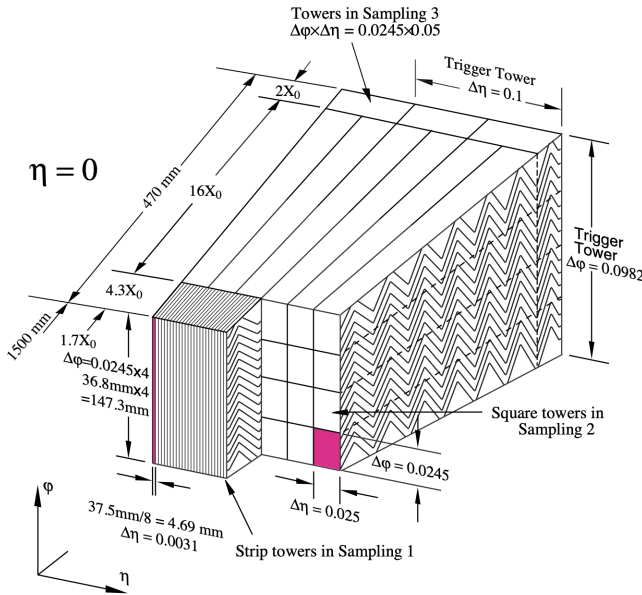


Figure 4.4: Diagram of a segment of the EMB, demonstrating the accordion plate arrangement [35]

594 released when a charged particle ionizes the liquid argon. In the barrel region, the electrons are
 595 driven towards the center electrodes by a 2000 V potential with a drift time of less than 450 ns [37].
 596 In the end-caps the voltage varies as a function of the radius in order to maintain a flat response
 597 [35]. The amount of current produced by the ionized electrons is proportional to the energy of
 598 the particle creating the signal. Figure 4.5 shows the shape of the signal produced in the LAr
 599 calorimeter, before and after it undergoes shaping during the readout process. The shaping of the
 600 pulse enforces a positive peak and a negative tail, which ensures that subsequence pulses can be
 601 separated with the precision required for the 25 ns LHC bunch spacing [35].

602 Hadronic End-cap Calorimeter

603 The HEC sits radially beyond the EMEC. The copper absorber plates in the HEC are oriented
 604 perpendicular to the beamline, with LAr as the active medium. Each end-cap is divided into two
 605 independent wheels; the inner wheel uses 25 mm copper plates, while the outer wheel uses 50 mm
 606 plates as a cost saving measure. In each wheel, the 8.5 mm plate gap is crossed by three parallel

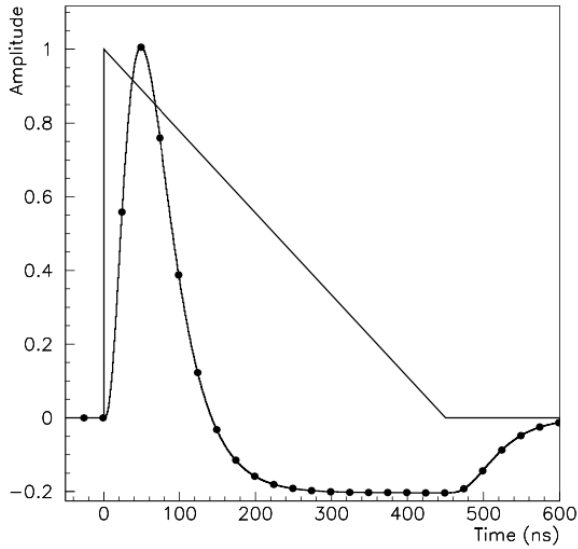


Figure 4.5: A LAr pulse as produced in the detector (triangle) and after shaping (curve) [35]

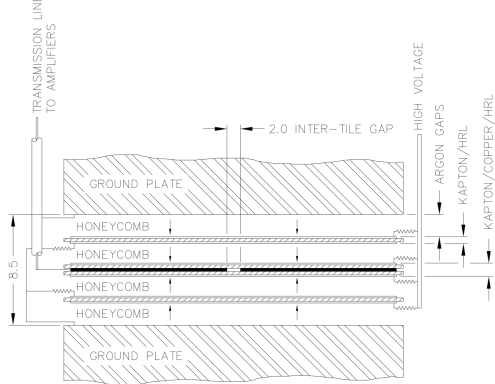


Figure 4.6: Readout gap structure in HEC [35]

607 electrodes, creating an effective drift distance of 1.8 mm. This gap is illustrated in Figure 4.6.
 608 Each wheel is divided into 32 wedge-shaped modules, each containing their own set of readout
 609 electronics.

610 **Forward Calorimeter**

611 The forward range is covered by the FCal, which provides both EM and hadronic calorimetry.
 612 It is composed of three active cylindrical modules; one EM module with copper absorber plates,
 613 and two hadronic modules with tungsten absorber plates. The plates are oriented perpendicular to

614 the beamline, and LAr is used as the active material throughout. The electrodes of the FCal consist
615 of tubes that run parallel to the beam line, arranged in a honeycomb pattern. The resulting LAr
616 gaps are as small as $250 \mu\text{m}$, which enables the FCal to handle the large influx of particles in the
617 forward region [35].

618 4.3.2 Tile Calorimeter

619 The Tile Calorimeter (TileCal) provides hadronic calorimetry in the region $\eta < 1.7$, and sur-
620 rounds the LAr calorimeter. It is responsible for measurements of jet energy and jet substructure,
621 and also plays an important role in electron isolation and triggering (including muons) [38]. Tile-
622 Cal is composed of 3 sections, as shown in Figure 4.3; a barrel calorimeter sits directly outside the
623 LAr EMB and provides coverage up to $\eta < 1.0$. Two extended barrel sections sit outside the LAr
624 endcaps and cover the region $0.8 < \eta < 1.7$.

625 TileCal is a sampling calorimeter composed of steel and plastic scintillator plates as illustrated
626 in Figure 4.7. A total of 460,000 scintillators are read out by wavelength-shifting fibers. The
627 fibers are gathered to define cells and in turn read out by photomultiplier tubes, which amplify
628 the signal and convert it to an electrical signature. Each cell has an approximate granularity of
629 $\Delta\eta \times \Delta\phi = 0.1 \times 0.1$. Each barrel is divided azimuthally into 64 independent modules, an example
630 of which is show in Figure 4.7. The modules are each serviced by front-end electronic housed in a
631 water-cooled drawer on the exterior of the module.

632 The detection principle of the TileCal is the production of light from hadronic particles inter-
633 acting with the scintillating tiles. When a hadronic particle hits the steel plate, a shower of particles
634 are produced. The interaction of the shower with the plastic scintillator produces photons, the num-
635 ber and intensity of which are proportional to the original particle's energy.

636

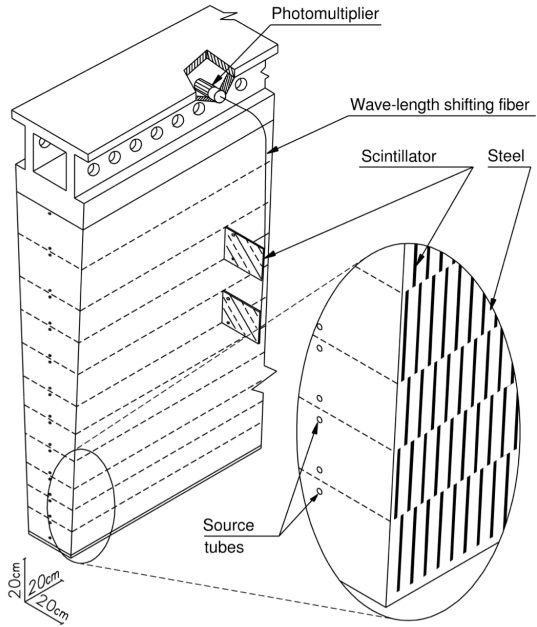


Figure 4.7: TileCal wedge module [38]

637 4.4 Muon Spectrometer

638 Unlike electrons, photons, and hadrons, muons interact minimally with the ATLAS calorimeters, and can pass through large amounts of detector material without stopping. The ATLAS Muon
 639 Spectrometer (MS) provides additional tracking information to improve the identification and measurement of muons. The MS comprises the outermost layers of the detector, and is interspersed
 640 with toroid magnets (discussed in Section 4.5), which provide a magnetic field of approximately
 641 0.5 T. The magnetic field bends the trajectory of the muons as they pass through the detector, and
 642 the degree of the bend is directly correlated with the muon momentum. The path of the muon is
 643 primarily measured by hits in three layers of Monitored Drift Tube (MDT) precision chambers,
 644 which cover the range $|\eta| < 2.7$. The barrel layout of the MS is show in Figure 4.8.

647 Muon triggering is provided by three layers of Resistive Plate Chambers (RPC) in the barrel
 648 ($|\eta| < 1.05$), and 3 - 4 layers of Thin Gap Chambers (TGC) in the end-caps ($1.05 < |\eta| < 2.4$).
 649 RPCs and TGCs also provide muon track measurements in the non-bending coordinate (ϕ). RPCs
 650 are constructed from two parallel resistive plates separated by a 2mm gap filled with a sensitive

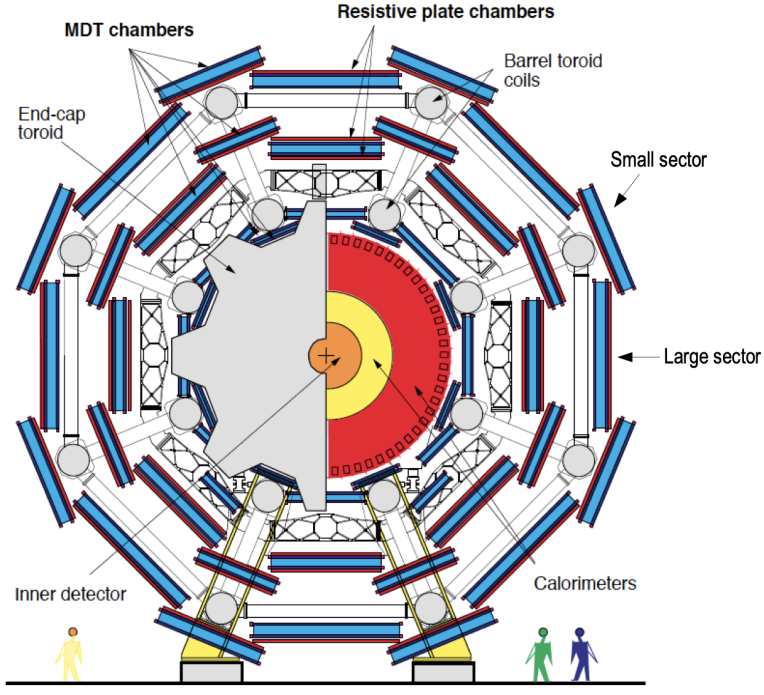


Figure 4.8: Cross section view of the muon spectrometer system [39]

651 gas mixture. This provides a total of six independent measurements for each muon track, with a
 652 spatial resolution of ~ 1 cm and a time resolution of ~ 1 ns. Time measurements from the RPCs
 653 are primarily associated to hits in the MDT precision chambers to determine the bunch crossing.
 654 The time measurement is also used to reject cosmic muons, and to search for delayed signals.
 655 TCGs provide triggering in the end-cap regions, and consist of parallel $30\ \mu\text{m}$ wires suspended
 656 in a sensitive gas mixture. TCGs provide high radiation tolerance and a fast response time, both
 657 features that are necessary for handling the high flux of muons in the forward region [39].

658 Precision measurements of muon momentum and position are primarily achieved by MDTs.
 659 The MDTs are constructed from 30 mm diameter tubes, permeated by a gas mixture of 93% Ar and
 660 7% CO₂. The average single-tube spatial resolution is $80\ \mu\text{m}$. Each chamber consists of six drift
 661 tube layers, which together provide a muon track segment resolution of $35\ \mu\text{m}$. The momentum
 662 of the muons can be calculated from the bend in the muon trajectory as they pass through the
 663 0.5T magnetic field provided by the toroids. For a $p_T = 1$ TeV track, the average p_T resolution is
 664 11%. In the inner most end-cap wheels, Cathode Strip Chambers (CSC) are used instead of MDTs,

665 covering the region $2.0 < |\eta| < 2.7$. CSCs are multi-wire proportional chambers, with a cathode
666 strip readout. The CSCs have a spatial resolution in the range of $50 \mu\text{m}$, and a maximum drift time
667 of about 30 ns, which makes them superior for handling the high flux of particles in the forward
668 region [40].

669 **4.5 Magnet System**

670 The ATLAS magnet system consists of four sets of superconducting magnets: a barrel solenoid,
671 a barrel toroid, and two end-cap toroids. The solenoid magnet produces a 2T magnetic field re-
672 sponsible for bending the trajectories of charged particles as they pass through the inner detector.
673 The three toroid magnets provide a field of 0.5 - 1 T and curve the path of muons passing through
674 the muon spectrometer.

675 The inner solenoid magnet is composed of over 9 km of niobium-titanium superconductor
676 wires, which are imbedded into strengthen pure aluminum strips. The solenoid is just 4.5 cm
677 thick, which minimizes interactions between the magnet material and particles passing through the
678 detector. It is housed in the LAr cryostat, as described in section 4.3.1, which further reduces the
679 amount of non-detector material required to support the solenoid. The return yoke of the magnet
680 is provided by the iron absorber of the TileCal [41].

681 The central ATLAS toroid magnet, providing the magnetic field for the barrel region of the MS,
682 is the largest toroidal magnet ever constructed at 25 m in length. The toroid is composed of eight
683 individual coils, each housed in their own cryostat. The toroidal magnetic field is advantageous
684 as the direction of the field is almost perpendicular to the path of the charged particles. 56 km of
685 aluminum stabilized niobium-titanium-copper superconductor wire compose the magnet. In each
686 end-cap, eight smaller superconducting coils extend the toroidal magnetic field to particles leaving
687 the detector in the forward direction [41]. Figure 4.9 shows the layout of the toroid magnets.

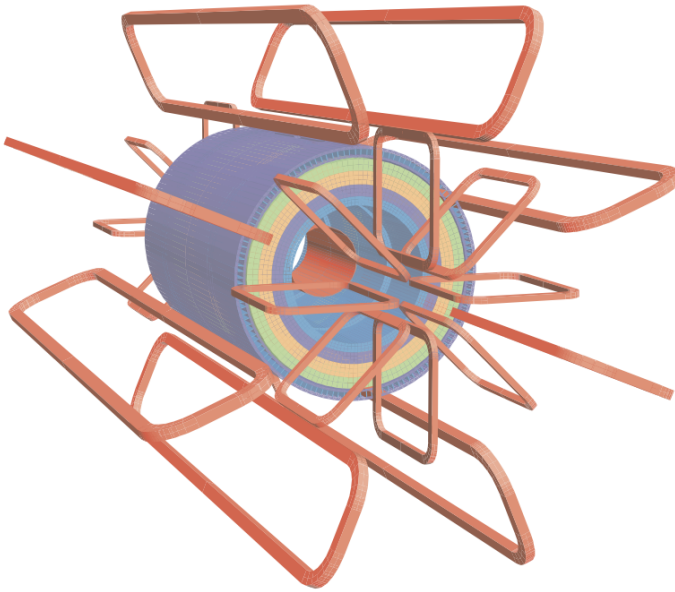


Figure 4.9: Layout of the barrel and endcap toroid magnets [32]

688 4.6 Forward Detectors

689 In addition to the inner detector, calorimeters, and muon spectrometer, three smaller detectors
690 provide coverage in the very forward region. The innermost forward detector, at 17 m from the
691 interaction point, is the **L**Uminosity measurement using **C**erenkov **I**ntegrating **D**etector (LUCID).
692 LUCID's primary purpose is to measure the relative online-luminosity for the ATLAS detector,
693 from inelastic $p - p$ scattering. The detector is composed of 20 aluminum Cerenkov tubes which
694 surround the beam pipe and face towards the interaction point.

695 The second forward detector is the Zero-Degree Calorimeter (ZDC), located 140 m from the
696 interaction point in both directions, at the point where the LHC beam-pipe divides into two separate
697 pipes. The ZDC's primary purpose is to detect forward neutrons from heavy ion collisions.

698 The third forward detector is the Absolute Luminosity For ATLAS (ALFA) system, located 240
699 m from the interaction point in both directions. ALFA determines luminosity by measuring elastic
700 scattering at small angles, from which luminosity can be calculated via the optical theorem. The
701 detector is built from scintillating fiber trackers. These are connected to the accelerator vacuum

702 via Roman pots, which allow the detector to come as close as 1mm to the beam without disrupting
703 the machine vacuum. The LUCID and ALFA detectors are crucial to determining the real-time
704 conditions of the beams and the total luminosity delivered to the ATLAS detector [32].

705 **4.7 Trigger and Data Acquisition**

706 The trigger and Data Acquisition systems (TDAQ) are responsible for selecting the most viable
707 events to save for further downstream processing. Because of the high luminosities delivered to
708 the ATLAS detector, not all events recorded can be saved; the 40 MHz bunch crossing rate must
709 be reduced by 5 orders of magnitude to an event storage rate of \sim 1 kHz. The trigger system is
710 composed of three distinct levels: Level 1 (L1), Level 2 (L2) and the event filter. Collectively the
711 L2 trigger and the event filter form the High Level Trigger (HLT).

712 The L1 trigger is implemented in the hardware of the ATLAS calorimeter and muon systems.
713 The primary modality of the L1 trigger is to identify muons, electrons, photons, jets, and τ -leptons
714 with high transverse momentum. Particles with high transverse momentum are more likely to
715 originate from direct, high energy collisions, which are most likely to produce interesting physics
716 processes. The L1 trigger also identifies events with large missing transverse energy, which could
717 be indicative of new physics. The L1 muon trigger (L1Muon) relies on RPC and TGC trigger
718 chambers in the barrel and end-cap regions of the muon spectrometer. The L1 Calorimeter Trigger
719 (L1Calo) uses reduced granularity information collected by all the calorimeter subsystems. Results
720 from the L1Muon and L1Calo triggers are combined by the Central Trigger Processor (CTP),
721 which implements a trigger ‘menu’, listing various combinations of trigger requirements. The
722 maximum L1 acceptance rate is 75 kHz, and the L1 trigger decision must reach the front-end
723 electronics within $2.5\ \mu s$ of its associated bunch-crossing [32].

724 The L1 trigger defines a Region-of-Interest (RoI) for each passing event. The ROI is repre-
725 sented by the η - ϕ detector region where interesting features were identified by the L1 selection
726 process. Information about the type of feature identified and the threshold which was exceeded to
727 trigger the L1 response is also recorded. The ROI data is sent to the L2 trigger, which uses all of

728 the available information within the ROI at full granularity and precision. The L2 trigger reduces
729 the event rate from 75 kHz to 3.5 kHz, with an average processing time of 40 ms. The final stage of
730 the HLT is the event filter, which reduces the event rate to 200 Hz. The event filter uses an offline
731 analysis process to select fully rebuilt events which will be saved for further analysis.

732 All levels of the ATLAS trigger system depend on specialized electronics. Each detector front-
733 end system has a specialized Readout Driver (ROD) which collects information from several front-
734 end data streams at once. The ROD is composed of front-end analogue processing, an L1 buffer
735 which retains the information long enough for the L1 trigger decision, and dedicated links which
736 send the front-end L1 triggered data to Data Acquisition System (DAQ). Any digital signals are
737 formatted as raw data before being transferred to the DAQ. The first stage of the DAQ temporarily
738 stores the L1 data in local buffers. The ROI data is then requested by the L2 trigger, after which
739 selected events are transferred to an event building system, before events passing the event filter
740 are sent to the CERN computer center for permanent storage. The DAQ system not only allows
741 for the readout of detector data, but is also responsible for the monitoring and configuration of
742 the hardware and software components which make up the data readout system via the Detector
743 Control System (DCS).

744 The DCS allows centralized control of all detector subsystems simultaneously. It continually
745 monitors operational conditions, reports any abnormal behavior to the operator, and can perform
746 both automatic and manual interventions. The DCS reports on real time detector conditions such
747 as high or low voltage detector electronics, gas and cooling systems, magnetic field conditions,
748 humidity and temperature. This information is continually monitored by experts in the ATLAS
749 control room, so that action can be taken immediately to correct any issues that arise. The DCS also
750 handles communication between detector systems, and other systems such as the LHC accelerator,
751 the ATLAS magnets, and CERN technical services [32].

Chapter 5: Particle Reconstruction and Identification

754 With a design luminosity of $1.0 \times 10^{34} \text{ cm}^{-2}\text{s}^{-1}$, and a peak Run-2 instantaneous luminosity of
 755 $2.0 \times 10^{34} \text{ cm}^{-2}\text{s}^{-1}$, reconstructing and identifying the products of LHC pp collisions is one of the
 756 most complex tasks for each LHC experiment. The accurate reconstruction and identification of
 757 physics objects lays the ground work for all subsequent physics analyses, so it is also one of the
 758 most fundamentally important tasks performed by an experiment.

759 Reconstruction is the process of combining raw and uncalibrated hits across various subsys-
 760 tems into specific unique objects. Two particular subsystems, the Inner Detector (ID) tracker and
 761 the calorimeter play particularly important roles and will be discussed in detail. Analysis of the
 762 properties of the reconstructed objects identifies them as photon, electrons, muons, or jets. While
 763 photons, electrons, and muons are fundamental particles, jets represent a collimated shower of
 764 many hadronic particles, whose definition is more flexible. Jet reconstruction, clustering and sub-
 765 structure are all of particular important to jet identification, and to the later content of this thesis.
 766 Finally, reconstruction also identifies missing transverse energy E_T^{miss} in events, which is a crucial
 767 variable for BSM physics searches. Figure 5.1 shows how the various physics objects listed here
 768 interact with various systems in the ATLAS detector.

769 5.1 Inner Detector Tracks

770 As the inner most layer of the detector, the ID measures charged particles close to the interac-
 771 tion point. The various hits of these charged particles throughout the ID are used to reconstruct
 772 *tracks* which give the trajectories of charged particles. Track reconstruction begins by clustering
 773 hits in the Pixel and SCT detectors, and combining clusters from different radial layers of these de-
 774 tector. The multi-layer clusters form track *seeds*, which provide initial estimates of measurements

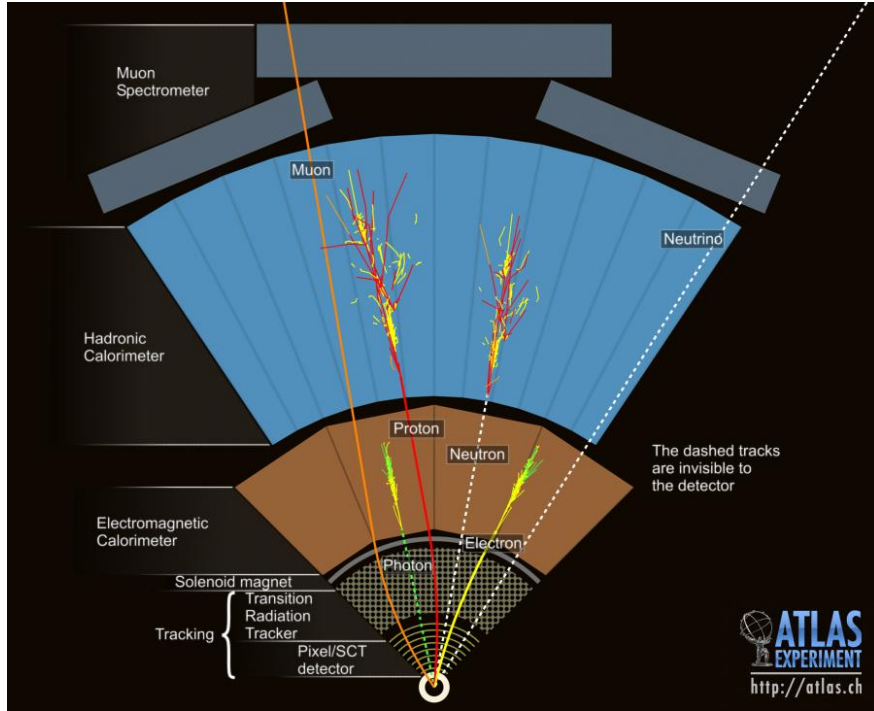


Figure 5.1: Graphic illustrating the various objects and high level features identified by ATLAS object reconstruction, and their interaction with different systems of the ATLAS detector [42]

775 belonging to an individual track. The requirement of three points allows for a rough estimate of
 776 the track p_T to be made by calculating the curvature of the track and accounting of the magnetic
 777 field in the ID.

778 Tracks seeds are subject to a variety of quality requirements, such as having a minimum esti-
 779 mated p_T and passing interaction region compatibility criterion. If these requirements are satisfied,
 780 the track seeds are passed to the track finding and fitting algorithms. The interplay of these three
 781 track reconstruction steps is illustrated in Figure 5.2.

782 5.2 Photons and Electrons

783 Photons and electrons shower in the LAr calorimeter, and are identified by the energy deposits
 784 they leave there. Energy deposits in a collection of nearby cells are termed *clusters*, which become
 785 the starting point for electron and photon reconstruction [44]. The clustering algorithm begins
 786 when the energy deposit in a certain cell exceeds the noise threshold with a significance of 4σ .

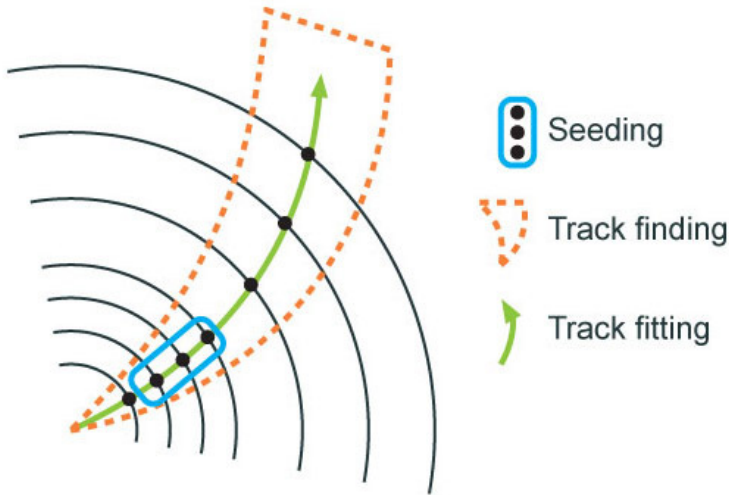


Figure 5.2: Track reconstruction seeding, finding and fitting illustration [43]

787 The algorithm then collects neighboring cells which have an energy deposit exceeding the noise
 788 threshold with a significance of 2σ , creating a topo-cluster. Next, these topo-clusters are matched
 789 to ID tracks, created as described in Section 5.1. The location of the topo-cluster defines a region
 790 of interest (ROI) in the ID, where additional modified track reconstruction algorithms are run in the
 791 case that no associated tracks are found. Any ID tracks associated to the topo-cluster are retrofitted to
 792 allow for additional energy loss due to bremsstrahlung. A converted photon track reconstruction
 793 algorithm is run to check for tracks coming from secondary vertices consistent with converted
 794 photons. The secondary vertices are constructed from two opposite charged tracks consistent with
 795 a massless particle, or from one track without any hits in the innermost layer of the ID.

796 For electron identification, the EM cluster is required to match ID tracks that originate from
 797 the primary vertex at the interaction point. For photon identification, the EM cluster can either be
 798 matched to tracks coming from a secondary vertex (converted photon), or matched to no tracks
 799 (unconverted photon). Figure 5.3 illustrates these three cases for EM object identification.

800 *Superclusters* are built separately for photons and electrons, based on the combined topo-cluster
 801 and ID track information. First, the EM topo-clusters are tested to see if they meet the minimum
 802 requirements to become electron or photon seed clusters. For electrons, the cluster must have a
 803 minimum E_T of 1 GeV, and must be matched to a track with at least 4 hits in the silicon tracking

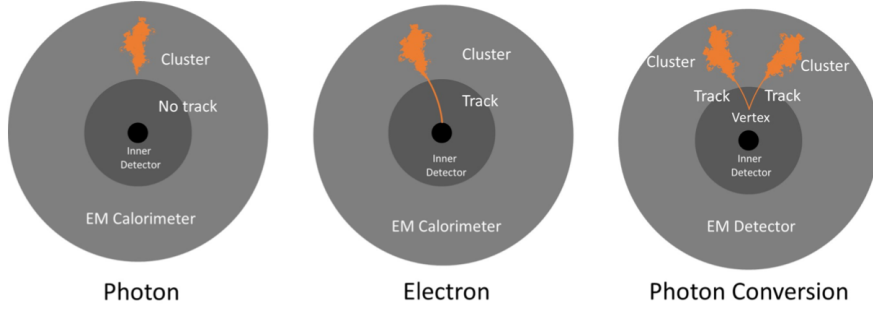


Figure 5.3: Four types of muon track candidates [45].

detectors. For photons, the cluster must have an E_T greater than 1.5 GeV. If the seed cluster requirements are met, the algorithm searches for satellite clusters, which can arise from bremsstrahlung radiation. If the satellite clusters pass the positional, energy and tracking requirements to be associated with the proto-cluster, they are combined into a supercluster.

Electron and photon objects are identified from the superclusters after energy calibration and position corrections are applied. Because photon and electron superclusters are built independently, some clusters can produce both a photon and an electron. In this case an ambiguity resolution procedure is applied to determine if the supercluster can be easily identified as only a photon (no tracks present) or only an electron (good tracks pointing to the primary vertex). In some cases, the identity of the cluster is still ambiguous, in which case both a photon and electron object are created for analysis and flagged as ambiguous. Energy, shower shape, and other analysis variables are calculated from the supercluster and saved with the electron or photon object.

5.3 Muons

Muons are identified through the tracks and energy deposits they leave in the ID, calorimeters, and Muon Spectrometer (MS). Muon identification begins in the Muon Drift Tube chambers by performing a straight line fit between the hits found in each layer, creating *segments*. Segments in the middle layers are then used as seeds for the track building algorithm, which searches for compatible combinations of segments based on their relative positions and angles. A χ^2 fit is

822 performed on each track candidate [46]. Based on the χ^2 criteria, hits are removed or added such
823 that the track contains as many hits as possible while satisfying the fit criteria.

824 The MS track candidates are combined with track information from the ID and calorimeters
825 according to various algorithms based on the information available from each subdetector. Four
826 different types of muons arise from the various reconstruction algorithms:

- 827 • Combined muon: a muon track identified through independent track reconstruction in the
828 ID and MS, where the combined track is formed using a global refit that uses hit information
829 from both detectors. Most muons are constructed through an outside-in procedure, in which
830 a muon track candidate is identified in the MS and then an associated track is found in the ID.
831 A complementary inside-out procedure is also implemented and identifies additional muons.
- 832 • Segment-tagged muon: an ID track is identified as a muon if when extrapolated out to the
833 MS (following the inside-out global fit procedure) it is matched to at least one local MS
834 segment.
- 835 • Calorimeter-tagged muon: an ID track is identified as a muon if it is matched to a calorimeter
836 energy deposit that is compatible with a minimum-ionizing particle. This muon identifica-
837 tion has the lowest purity, but it used in regions where the MS has only partial coverage due
838 to cabling and service access routes.
- 839 • Extrapolated muons: the muon is reconstruction only from the MS track and a requirement
840 on compatibility with the primary interaction point. The muon track is required to cross at
841 least two layers of the MS, and three layers in the forward region. These muons are mainly
842 used to extend muon acceptance into the region $2.5 < |\eta| < 2.7$ where ID track information
843 is not available.

844 Figure 5.4 illustrates the four types of muon reconstruction. Overlap between reconstructed
845 muons using ID tracks is resolved by giving preference to combined muons, then segment tagged
846 muons, and finally calorimeter tagged muons. Overlap with extrapolated muons is resolved by
847 giving preference to the muon with a better fit quality and higher number of tracks.

848 All muon track candidates are required to pass a series of quality selections to be identified in
849 the final muon collection. The primary qualities considered are the χ^2 goodness of fit for the global
850 track, the difference in p_T measurement between the ID and MS tracks, and the ratio between the
851 charge and momentum of the tracks. The quality requirements help reject hadrons, primarily from
852 kaon and pion decays. Muons candidates consistent with cosmic rays are also rejected.

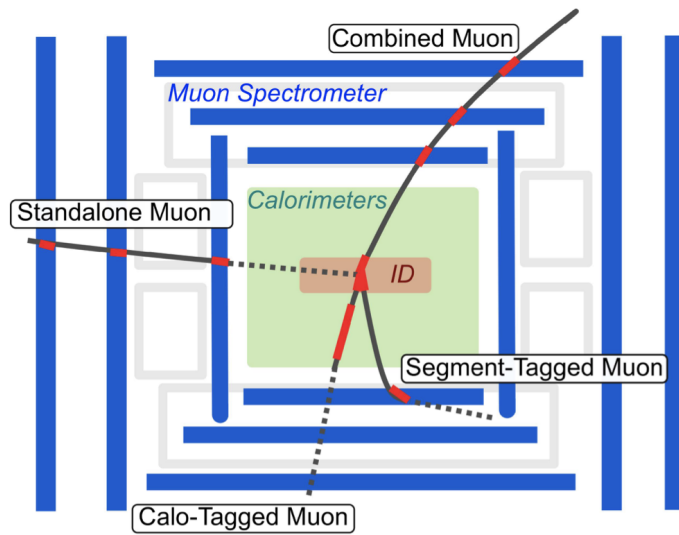


Figure 5.4: Four types of muon track candidates [47].

853 5.4 Jets

854 5.4.1 Calorimeter Clusters

855 5.4.2 Particle Flow Reconstruction

856 5.4.3 Jet Clustering

857 5.4.4 Jet Substructure

858 5.5 Missing Transverse Energy

Conclusion or Epilogue

860 Use this page for your epilogue or conclusion if applicable; please use only one of the titles
861 for this page. Otherwise, you may delete it. Use this page for your epilogue or conclusion if
862 applicable; please use only one of the titles for this page. Otherwise, you may delete it. Use this
863 page for your epilogue or conclusion if applicable; please use only one of the titles for this page.
864 Otherwise, you may delete it. Use this page for your epilogue or conclusion if applicable; please
865 use only one of the titles for this page. Otherwise, you may delete it. Use this page for your
866 epilogue or conclusion if applicable; please use only one of the titles for this page. Otherwise,
867 you may delete it. Use this page for your epilogue or conclusion if applicable; please use only one
868 of the titles for this page. Otherwise, you may delete it. Use this page for your epilogue or
869 conclusion if applicable; please use only one of the titles for this page. Otherwise, you may delete
870 it. Use this page for your epilogue or conclusion if applicable; please use only one of the titles for
871 this page. Otherwise, you may delete it. Use this page for your epilogue or conclusion if
872 applicable; please use only one of the titles for this page. Otherwise, you may delete it. Use this
873 page for your epilogue or conclusion if applicable; please use only one of the titles for this page.
874 Otherwise, you may delete it. Use this page for your epilogue or conclusion if applicable; please
875 use only one of the titles for this page. Otherwise, you may delete it. Use this page for your
876 epilogue or conclusion if applicable; please use only one of the titles for this page. Otherwise,
877 you may delete it. Use this page for your epilogue or conclusion if applicable; please use only one
878 of the titles for this page. Otherwise, you may delete it. Use this page for your epilogue or
879 conclusion if applicable; please use only one of the titles for this page. Otherwise, you may delete

880 it. Use this page for your epilogue or conclusion if applicable; please use only one of the titles for
881 this page. Otherwise, you may delete it. Use this page for your epilogue or conclusion if
882 applicable; please use only one of the titles for this page. Otherwise, you may delete it. Use this
883 page for your epilogue or conclusion if applicable; please use only one of the titles for this page.
884 Otherwise, you may delete it. Use this page for your epilogue or conclusion if applicable; please
885 use only one of the titles for this page. Otherwise, you may delete it. Use this page for your
886 epilogue or conclusion if applicable; please use only one of the titles for this page. Otherwise,
887 you may delete it. Use this page for your epilogue or conclusion if applicable; please use only one
888 of the titles for this page. Otherwise, you may delete it. Use this page for your epilogue or
889 conclusion if applicable; please use only one of the titles for this page. Otherwise, you may delete
890 it. Use this page for your epilogue or conclusion if applicable; please use only one of the titles for
891 this page. Otherwise, you may delete it. Use this page for your epilogue or conclusion if
892 applicable; please use only one of the titles for this page. Otherwise, you may delete it. Use this
893 page for your epilogue or conclusion if applicable; please use only one of the titles for this page.
894 Otherwise, you may delete it. Use this page for your epilogue or conclusion if applicable; please
895 use only one of the titles for this page. Otherwise, you may delete it. Use this page for your
896 epilogue or conclusion if applicable; please use only one of the titles for this page. Otherwise,
897 you may delete it. Use this page for your epilogue or conclusion if applicable; please use only one
898 of the titles for this page. Otherwise, you may delete it. Use this page for your epilogue or
899 conclusion if applicable; please use only one of the titles for this page. Otherwise, you may delete
900 it. Use this page for your epilogue or conclusion if applicable; please use only one of the titles for
901 this page. Otherwise, you may delete it. Use this page for your epilogue or conclusion if
902 applicable; please use only one of the titles for this page. Otherwise, you may delete it. Use this
903 page for your epilogue or conclusion if applicable; please use only one of the titles for this page.
904 Otherwise, you may delete it. Use this page for your epilogue or conclusion if applicable; please
905 use only one of the titles for this page. Otherwise, you may delete it. Use this page for your
906 epilogue or conclusion if applicable; please use only one of the titles for this page. Otherwise,

907 you may delete it. Use this page for your epilogue or conclusion if applicable; please use only one
908 of the titles for this page. Otherwise, you may delete it. Use this page for your epilogue or
909 conclusion if applicable; please use only one of the titles for this page. Otherwise, you may delete
910 it. Use this page for your epilogue or conclusion if applicable; please use only one of the titles for
911 this page. Otherwise, you may delete it. Use this page for your epilogue or conclusion if
912 applicable; please use only one of the titles for this page. Otherwise, you may delete it. Use this
913 page for your epilogue or conclusion if applicable; please use only one of the titles for this page.
914 Otherwise, you may delete it. Use this page for your epilogue or conclusion if applicable; please
915 use only one of the titles for this page. Otherwise, you may delete it. Use this page for your
916 epilogue or conclusion if applicable; please use only one of the titles for this page. Otherwise,
917 you may delete it. Use this page for your epilogue or conclusion if applicable; please use only one
918 of the titles for this page. Otherwise, you may delete it. Use this page for your epilogue or
919 conclusion if applicable; please use only one of the titles for this page. Otherwise, you may delete
920 it. Use this page for your epilogue or conclusion if applicable; please use only one of the titles for
921 this page. Otherwise, you may delete it. Use this page for your epilogue or conclusion if
922 applicable; please use only one of the titles for this page. Otherwise, you may delete it. Use this
923 page for your epilogue or conclusion if applicable; please use only one of the titles for this page.
924 Otherwise, you may delete it. Use this page for your epilogue or conclusion if applicable; please
925 use only one of the titles for this page. Otherwise, you may delete it. Use this page for your
926 epilogue or conclusion if applicable; please use only one of the titles for this page. Otherwise,
927 you may delete it. Use this page for your epilogue or conclusion if applicable; please use only one
928 of the titles for this page. Otherwise, you may delete it. Use this page for your epilogue or
929 conclusion if applicable; please use only one of the titles for this page. Otherwise, you may delete
930 it. Use this page for your epilogue or conclusion if applicable; please use only one of the titles for
931 this page. Otherwise, you may delete it. Use this page for your epilogue or conclusion if
932 applicable; please use only one of the titles for this page. Otherwise, you may delete it. Use this
933 page for your epilogue or conclusion if applicable; please use only one of the titles for this page.

934 Otherwise, you may delete it. Use this page for your epilogue or conclusion if applicable; please
935 use only one of the titles for this page. Otherwise, you may delete it. Use this page for your
936 epilogue or conclusion if applicable; please use only one of the titles for this page. Otherwise,
937 you may delete it. Use this page for your epilogue or conclusion if applicable; please use only one
938 of the titles for this page. Otherwise, you may delete it. Use this page for your epilogue or
939 conclusion if applicable; please use only one of the titles for this page. Otherwise, you may delete
940 it. Use this page for your epilogue or conclusion if applicable; please use only one of the titles for
941 this page. Otherwise, you may delete it. Use this page for your epilogue or conclusion if
942 applicable; please use only one of the titles for this page. Otherwise, you may delete it. Use this
943 page for your epilogue or conclusion if applicable; please use only one of the titles for this page.
944 Otherwise, you may delete it. Use this page for your epilogue or conclusion if applicable; please
945 use only one of the titles for this page. Otherwise, you may delete it. Use this page for your
946 epilogue or conclusion if applicable; please use only one of the titles for this page. Otherwise,
947 you may delete it. Use this page for your epilogue or conclusion if applicable; please use only one
948 of the titles for this page. Otherwise, you may delete it. Use this page for your epilogue or
949 conclusion if applicable; please use only one of the titles for this page. Otherwise, you may delete
950 it. Use this page for your epilogue or conclusion if applicable; please use only one of the titles for
951 this page. Otherwise, you may delete it. Use this page for your epilogue or conclusion if
952 applicable; please use only one of the titles for this page. Otherwise, you may delete it. Use this
953 page for your epilogue or conclusion if applicable; please use only one of the titles for this page.
954 Otherwise, you may delete it. Use this page for your epilogue or conclusion if applicable; please
955 use only one of the titles for this page. Otherwise, you may delete it. Use this page for your
956 epilogue or conclusion if applicable; please use only one of the titles for this page. Otherwise,
957 you may delete it. Use this page for your epilogue or conclusion if applicable; please use only one
958 of the titles for this page. Otherwise, you may delete it. Use this page for your epilogue or
959 conclusion if applicable; please use only one of the titles for this page. Otherwise, you may delete
960 it.

References

- [1] Jens Erler and Paul Langacker. “Electroweak model and constraints on new physics”. In: (July 2004). arXiv: hep-ph/0407097.
- [2] David J Griffiths. *Introduction to elementary particles; 2nd rev. version*. Physics textbook. New York, NY: Wiley, 2008.
- [3] M. Tanabashi et al. “Review of Particle Physics”. In: *Phys. Rev. D* 98 (3 2018), pp. 847–851.
- [4] E. Noether. “Invariante Variationsprobleme”. In: *Nachr. d. König. Gesellsch. d. Wiss. zu Göttingen, Math-phys. Klasse*, Seite 235-157 (1918). eprint: www.physics.ucla.edu/\~\cwp/articles/noether.trans/german/emmy235.html.
- [5] J. H. Christenson et al. “Evidence for the 2π Decay of the K_2^0 Meson”. In: *Phys. Rev. Lett.* 13 (1964), pp. 138–140.
- [6] J. E. Augustin et al. “Discovery of a Narrow Resonance in e^+e^- Annihilation”. In: *Phys. Rev. Lett.* 33 (1974), pp. 1406–1408.
- [7] J. J. Aubert et al. “Experimental Observation of a Heavy Particle J ”. In: *Phys. Rev. Lett.* 33 (1974), pp. 1404–1406.
- [8] Martin L. Perl et al. “Evidence for Anomalous Lepton Production in e+ - e- Annihilation”. In: *Phys. Rev. Lett.* 35 (1975), pp. 1489–1492.
- [9] S. W. Herb et al. “Observation of a Dimuon Resonance at 9.5-GeV in 400-GeV Proton-Nucleus Collisions”. In: *Phys. Rev. Lett.* 39 (1977), pp. 252–255.
- [10] F. Abe et al. “Observation of top quark production in $\bar{p}p$ collisions”. In: *Phys. Rev. Lett.* 74 (1995), pp. 2626–2631. arXiv: hep-ex/9503002.
- [11] S. Abachi et al. “Observation of the top quark”. In: *Phys. Rev. Lett.* 74 (1995), pp. 2632–2637. arXiv: hep-ex/9503003.
- [12] K. Kodama et al. “Observation of tau neutrino interactions”. In: *Phys. Lett. B* 504 (2001), pp. 218–224. arXiv: hep-ex/0012035.
- [13] G. Arnison et al. “Experimental Observation of Lepton Pairs of Invariant Mass Around 95-GeV/c**2 at the CERN SPS Collider”. In: *Phys. Lett. B* 126 (1983), pp. 398–410.

- 988 [14] P. Bagnaia et al. “Evidence for $Z^0 \rightarrow e^+e^-$ at the CERN $\bar{p}p$ Collider”. In: *Phys. Lett. B* 129
 989 (1983), pp. 130–140.
- 990 [15] Serguei Chatrchyan et al. “Observation of a New Boson at a Mass of 125 GeV with the
 991 CMS Experiment at the LHC”. In: *Phys. Lett. B* 716 (2012), pp. 30–61. arXiv: 1207.7235
 992 [hep-ex].
- 993 [16] Georges Aad et al. “Observation of a new particle in the search for the Standard Model
 994 Higgs boson with the ATLAS detector at the LHC”. In: *Phys. Lett. B* 716 (2012), pp. 1–29.
 995 arXiv: 1207.7214 [hep-ex].
- 996 [17] K. G. Begeman, A. H. Broeils, and R. H. Sanders. “Extended rotation curves of spiral galax-
 997 ies: Dark haloes and modified dynamics”. In: *Mon. Not. Roy. Astron. Soc.* 249 (1991), p. 523.
- 998 [18] Y. Ashie et al. “Evidence for an oscillatory signature in atmospheric neutrino oscillation”.
 999 In: *Phys. Rev. Lett.* 93 (2004), p. 101801. arXiv: hep-ex/0404034.
- 1000 [19] C. Abel et al. “Measurement of the Permanent Electric Dipole Moment of the Neutron”. In:
 1001 *Phys. Rev. Lett.* 124.8 (2020), p. 081803. arXiv: 2001.11966 [hep-ex].
- 1002 [20] Guillaume Albouy et al. “Theory, phenomenology, and experimental avenues for dark show-
 1003 ers: a Snowmass 2021 report”. In: *The European Physical Journal C* 82.12 (Dec. 2022).
- 1004 [21] Lyndon Evans and Philip Bryant. “LHC Machine”. In: *Journal of Instrumentation* 3.08
 1005 (2008), S08001.
- 1006 [22] “The ATLAS Experiment at the CERN Large Hadron Collider”. In: *JINST* 3 (2008). Also
 1007 published by CERN Geneva in 2010, S08003.
- 1008 [23] “The CMS experiment at the CERN LHC”. In: *Journal of Instrumentation* 3.08 (2008),
 1009 S08004.
- 1010 [24] “The ALICE experiment at the CERN LHC”. In: *Journal of Instrumentation* 3.08 (2008),
 1011 S08002.
- 1012 [25] “The LHCb Detector at the LHC”. In: *Journal of Instrumentation* 3.08 (2008), S08005.
- 1013 [26] Ana Lopes and Melissa Loyse Perrey. *FAQ-LHC The guide*. 2022.
- 1014 [27] Esma Mobs. “The CERN accelerator complex in 2019. Complexe des accélérateurs du
 1015 CERN en 2019”. In: (2019). General Photo.
- 1016 [28] *Pulling together: Super Conducting electromagnets*. <https://home.cern/science/engineering/pulling-together-superconducting-electromagnets>.
 1017 Accessed: 2024-01-05.

- 1019 [29] *The High-Luminosity LHC*. <https://voisins.web.cern.ch/en/high-luminosity-lhc-hl-lhc>. Accessed: 2024-01-05.
- 1020
- 1021 [30] Aad G., et al. (ATLAS Collaboration and CMS Collaboration). “Combined Measurement of
1022 the Higgs Boson Mass in pp Collisions at $\sqrt{s} = 7$ and 8 TeV with the ATLAS and CMS
1023 Experiments”. In: *Phys. Rev. Lett.* 114 (19 2015), p. 191803.
- 1024 [31] O. Aberle et al. *High-Luminosity Large Hadron Collider (HL-LHC): Technical design re-*
1025 *port*. CERN Yellow Reports: Monographs. Geneva: CERN, 2020.
- 1026 [32] The ATLAS Collaboration. “The ATLAS Experiment at the CERN Large Hadron Collider”.
1027 In: *Journal of Instrumentation* 3.08 (2008), S08003.
- 1028 [33] G Aad, B Abbott, and ATLAS Collaboration. “Performance of the reconstruction of large
1029 impact parameter tracks in the inner detector of ATLAS”. In: *Eur. Phys. J. C Part. Fields*
1030 83.11 (Nov. 2023).
- 1031 [34] Joao Pequenao. *Computer Generated image of the ATLAS calorimeter*. 2008.
- 1032 [35] *ATLAS liquid-argon calorimeter: Technical Design Report*. Technical design report. AT-
1033 LAS. Geneva: CERN, 1996.
- 1034 [36] H A Gordon. “Liquid argon calorimetry for the SSC”. In: () .
- 1035 [37] Henric Wilkens and (on behalf of the ATLAS LArg Collaboration). “The ATLAS Liquid
1036 Argon calorimeter: An overview”. In: *Journal of Physics: Conference Series* 160.1 (2009),
1037 p. 012043.
- 1038 [38] *Technical Design Report for the Phase-II Upgrade of the ATLAS Tile Calorimeter*. Tech.
1039 rep. Geneva: CERN, 2017.
- 1040 [39] “Technical Design Report for the Phase-II Upgrade of the ATLAS Muon Spectrometer”. In:
1041 () .
- 1042 [40] L Pontecorvo. “The ATLAS Muon Spectrometer”. In: (2004). revised version number 1
1043 submitted on 2003-07-27 16:31:16.
- 1044 [41] *ATLAS magnet system: Technical Design Report, 1*. Technical design report. ATLAS. Geneva:
1045 CERN, 1997.
- 1046 [42] Joao Pequenao. “Event Cross Section in a computer generated image of the ATLAS detec-
1047 tor.” 2008.
- 1048 [43] ATLAS Collaboration. “ATLAS Experiment Implements Heterogeneous Particle Recon-
1049 struction with Intel oneAPI Tools”. General Photo. 2023.

- 1050 [44] ATLAS Collaboration. “Electron and photon performance measurements with the ATLAS
1051 detector using the 2015–2017 LHC proton-proton collision data”. In: *Journal of Instrumentation*
1052 14.12 (2019), P12006.
- 1053 [45] Chiara Deponte. “Studies on the properties of non-prompt photons at the ATLAS experi-
1054 ment”. Presented 16 Aug 2022. Technische Universitaet Dortmund (DE), 2022.
- [46] ATLAS Collaboration. “Muon reconstruction performance of the ATLAS detector in pro-
ton–proton collision data at
 \sqrt{s}
1055 $s = 13 \text{ TeV}$ ”. In: *The European Physical Journal C* 76.5 (2016).
- 1056 [47] Sebastien Rettie. *Muon identification and performance in the ATLAS experiment*. Tech. rep.
1057 Geneva: CERN, 2018.

1058

1059

Appendix A: Experimental Equipment

1060 Lorem ipsum dolor sit amet, consectetur adipiscing elit, sed do eiusmod tempor incididunt ut
1061 labore et dolore magna aliqua. Ut enim ad minim veniam, quis nostrud exercitation ullamco laboris
1062 nisi ut aliquip ex ea commodo consequat. Duis aute irure dolor in reprehenderit in voluptate velit
1063 esse cillum dolore eu fugiat nulla pariatur. Excepteur sint occaecat cupidatat non proident, sunt in
1064 culpa qui officia deserunt mollit anim id est laborum.

1065

1066

Appendix B: Data Processing

1067 Lorem ipsum dolor sit amet, consectetur adipiscing elit, sed do eiusmod tempor incididunt ut
1068 labore et dolore magna aliqua. Ut enim ad minim veniam, quis nostrud exercitation ullamco laboris
1069 nisi ut aliquip ex ea commodo consequat. Duis aute irure dolor in reprehenderit in voluptate velit
1070 esse cillum dolore eu fugiat nulla pariatur. Excepteur sint occaecat cupidatat non proident, sunt in
1071 culpa qui officia deserunt mollit anim id est laborum.